Change in frozen soils and the effects on regional hydrology, upper Heihe Basin, northeastern Qinghai-Tibetan Plateau

Bing Gao[1], Dawen Yang[2]*, Yue Qin[2], Yuhan Wang[2], Hongyi Li[3], Yanlin Zhang[3], and Tingjun Zhang[4]

[1] School of Water Resources and Environment, China University of Geosciences, Beijing 100083, China

[2] State Key Laboratory of Hydroscience and Engineering, Department of Hydraulic Engineering, Tsinghua University, Beijing 100084, China

[3] Cold and Arid Regions Environmental and Engineering Research Institute, Chinese Academy of Sciences, Lanzhou, Gansu 730000, China

[4] Key Laboratory of West China's Environmental Systems (MOE), College of Earth and Environmental Sciences, Lanzhou University, Lanzhou, 730000, China

Corresponding author: Dawen Yang (yangdw@tsinghua.edu.cn)

ABSTRACT:

Frozen ground has an important role in regional hydrological cycles and ecosystems, particularly on the Qinghai-Tibetan Plateau (QTP), which is characterized by high elevations and a dry climate. This study modified a distributed, physically-based hydrological model and applied it to simulate long-term (1971-2013) changes in frozen ground and the effects on hydrology in the upper Heihe basin, northeastern QTP. The model was validated against data obtained from multiple ground-based observations. Based on model simulations, we analyzed spatio-temporal changes in frozen soils and their effects on hydrology. Our results show that the area with permafrost shrank by 8.8% (approximately 500 km^2), predominantly in areas with elevations between 3500 m and 3900 m. The maximum depth of seasonally frozen ground decreased at a rate of approximately 0.032 m·decade^{-1}, and the active layer thickness over the permafrost increased by approximately 0.043 m·decade^{-1}. Runoff increased significantly during the cold season (November-March) due to an increase in liquid soil moisture caused by rising soil temperatures. Areas in which permafrost changed into seasonally frozen ground at high elevations showed especially large increases in runoff. Annual runoff increased due to increased precipitation, the base flow increased due to changes in frozen soils, and the actual evapotranspiration increased significantly due to increased precipitation and soil warming. The groundwater storage showed an increasing trend, indicating that a reduction in permafrost extent enhanced the groundwater recharge.

KEYWORDS: permafrost; seasonally frozen ground; soil moisture; ground temperature; runoff

1. Introduction

Global warming has led to significant changes in frozen soils, including both permafrost and seasonally frozen ground at high latitudes and high elevations (Hinzman et al., 2013; Cheng and Wu, 2007). Changes in frozen soils can greatly affect land-atmosphere interactions and the energy and water balances of the land surface (Subin et al., 2013; Schuur et al., 2015), altering soil moisture, water flow pathways and stream flow regimes (Walvoord and Kurylyk, 2016). Understanding the changes in frozen soils and their impacts on regional hydrology is important for water resources management and ecosystem protection in cold regions.

Previous studies based on either experimental observations or long-term meteorological or hydrological observations have examined changes in frozen soils and their impacts on hydrology. Several studies reported that permafrost thawing might enhance base flow in the Arctic and the Subarctic (Walvoord and Striegl, 2007; Jacques and Sauchyn, 2009; Ye et al., 2009), as well as in northeastern China (Liu et al., 2003; Duan et al., 2017). A few studies reported that permafrost thawing might reduce river runoff (here, runoff is defined as all liquid water flowing out of the study area), especially on the Qinghai-Tibetan Plateau (QTP) (e.g., Qiu, 2012; Jin et al., 2009). Those studies that include intensive field observations of frozen soils have typically been performed at small spatial scales over short periods (e.g., Cheng and Wu, 2007; Wu et al., 2010). Consequently, regional patterns and long-term trends are not typically captured. Long-term meteorological and hydrological observations are available in many areas, but they do not provide information on soil freezing and thawing processes

(McClelland et al., 2004; Liu et al., 2003; Niu et al., 2011). Therefore, previous observation-based studies have not provided a sufficient understanding of the long-term changes in frozen soils and their impact on regional hydrology (Woo et al., 2008).

As an alternative strategy, hydrological models have been coupled with soil freezing-thawing schemes to simulate impacts of the changes in frozen soils on catchment hydrology. Several hydrological models (Rawlins et al., 2003; Chen et al., 2008) used simple freezing-thawing schemes, but these cannot simulate the vertical soil temperature profiles. The modified VIC model (Cherkauer and Lettenmaier, 1999) and the CLM model (Oleson et al., 2010) simulate vertical soil freezing-thawing processes, but they simplify the flow routing using linear schemes. Subin et al. (2013) and Lawrence et al. (2015) used the CLM model to simulate global changes in permafrost. Cuo et al. (2015) used the VIC to simulate frozen soil changes and their hydrological impacts at the plot scale in the headwaters of the Yellow River. The GEOtop model (Endrizzi et al., 2014) simulates three-dimensional water flux and vertical heat transfer in soil, but it is difficult to apply to regional investigations. Wang et al. (2010) and Zhang et al. (2013) incorporated frozen soil schemes in a distributed hydrological model and showed improved performance in a small mountainous catchment. More regional studies are necessary to better understand the frozen soil changes and their impacts on regional hydrologic processes and water resources.

The QTP is known as Asia's water tower, and runoff changes on the plateau have significant impacts on water security in downstream regions (Walter et al., 2010); hence, such changes have attracted considerable attention in recent years (Cuo et al., 2014).

84   The QTP is characterized by high elevations and a cold climate. Consequently,

85   cryospheric processes have great impacts on its hydrological processes (Cheng and Jin,

86   2013; Cuo et al., 2014). The thickness of permafrost on the QTP varies from 1 to 130

87   m, and the temperature ranges between -0.5 and -3.5 ℃ (Yang et al., 2010). Compared

88   with Arctic and Subarctic soils, the frozen soils on the QTP are more sensitive to

89   increased air temperature (Yang et al., 2010), and changes in the frozen soils may have

90   more significant impacts on the regional hydrology.

91   Clear increases in annual and seasonal air temperatures have been observed on the

92   QTP (Li et al., 2005; Liu and Chen, 2000; Zhao et al., 2004). Several studies have

93   shown changes in frozen soils based on long-term observations. For example, Cheng

94   and Wu (2007) analyzed soil temperature profiles from boreholes on the QTP and found

95   that the active layer thickness of frozen soils increased by 0.15-0.50 m during the period

96   of 1996-2001. Zhao et al. (2004) observed a decreasing trend of freezing depth in the

97   seasonally frozen soils at 50 stations. Several studies have analyzed the relationship

98   between changes in frozen soils and river discharge using observational data (Zhang et

99   al., 2003; Jin et al., 2009; Niu et al., 2011). However, the spatio-temporal characteristics

100   of the long-term changes in frozen soils are not sufficiently clear. Based on

101   comprehensive field experiments (Cheng et al., 2014), a hydrological model coupling

102   cryospheric processes and hydrological processes has been developed (Yang et al., 2015;

103   Gao et al., 2016). This model provides a basis upon which to analyze the spatio-

104   temporal changes in frozen soils and their impacts on the regional hydrology in the

105   upper Heihe basin, northeastern QTP. Specifically, this study aims to: (1) explore the

106   spatial and temporal changes in frozen soils using a distributed hydrological model with

107   comprehensive validation and (2) analyze the hydrological responses to the changes in

108   frozen soils during the past 40 years in the upper Heihe basin.

109   **2.   Study Area and Data**

110   The Heihe River is one of the major inland basins in northwestern China. As shown in

111   Figure 1, the upper reaches of the Heihe River, representing a drainage area of 10,009

112   km^2, are located on the northeastern QTP at elevations ranging from 2200 to 5000 m.

113   The upper reaches of this river provide the majority of the water supplied to the middle

114   and lower reaches (Cheng et al., 2014). The annual precipitation in the upper Heihe

115   basin ranges from 200 to 700 mm, and the mean annual air temperature ranges from -9

116   to 5 ºC. Permafrost dominates the high elevation region above 3700 m (Wang et al.,

117   2013), and seasonal frozen ground covers the remaining portion of the study area.

118   Glaciers are found at elevations above 4000 m and cover approximately 0.8% of the

119   upper Heihe basin. The upper Heihe basin contains two tributaries, each with a

120   hydrological station; one at Qilian (on the eastern tributary) and the other at Zhamashike

121   (on the western tributary). The outlet of the upper Heihe basin also features a

122   hydrological station, namely, Yingluoxia (Figure 1).

123   The spatial data used in this study includes atmospheric forcing data, land surface

124   data and actual evapotranspiration data based on remote sensing. The atmospheric

125   forcing data include a 1-km gridded dataset of daily precipitation, air temperature,

126   sunshine hours, wind speed and relative humidity. The gridded daily precipitation was

127   interpolated from observations at meteorological stations (Figure 1) provided by the

128   China Meteorological Administration (CMA) using the method developed by Wang et

129   al. (2017). The other atmospheric forcing data were interpolated from observations at

130   meteorological stations using the inverse distance weighted method. The interpolation

131   of air temperature considers the elevation-dependent temperature gradient provided by

132   the HiWATER experiment (Li et al., 2013).

133   The land surface data used to run the model include land use, topography, leaf area

134   index (LAI), and soil parameters. The topography data were obtained from the Shuttle

135   Radar Topography Mission (SRTM) dataset (Jarvis et al., 2008) with a spatial resolution

136   of 90 m. The land use/cover data were provided by the Institute of Botany, Chinese

137   Academy of Sciences (Zhou and Zheng, 2014). The LAI data with 1-km resolution

138   were developed by Fan (2014). The soil parameters were developed by Song et al.

139   (2016) and include the saturated hydraulic conductivity, residual soil moisture content,

140   saturated soil moisture content, soil sand content, soil clay content and soil organic

141   content. Monthly actual evapotranspiration data with 1-km resolution during the period

142   of 2002-2012 were estimated based on remote sensing data (Wu et al., 2012; Wu, 2013).

143   The field observation data used in this study include river discharge, soil

144   temperature, frozen depth, soil moisture and borehole observations. Daily river

145   discharge data were obtained from the Hydrology and Water Resources Bureau of

146   Gansu Province. The CMA provided daily soil temperature data collected at the Qilian

147   station from January 1, 2004 to December 31, 2013, and daily frozen depth data

148   collected at the Qilian and Yeniugou stations from January 1, 2002 to December 31,

149   2013. We obtained ground temperature observations from six boreholes, whose location

150   are shown in Figure 1, from Wang et al. (2013). We used the observations at specific

151   dates instead of annual averages due to a lack of continuous measurements. The

152   borehole depths are 100 m for T1, 69 m for T2, 50 m for T3, 90 m for T4, and 20 m for

153   T5 and T7. The HiWATER experiment (Li et al., 2013; Liu et al., 2011) provided the

154   soil moisture data from January 1 to December 31, 2014 at the A'rou Sunny Slope

155   station (100.52 E, 38.09 N).

156   **3.   Methodology**

157   **3.1 Brief introduction of the hydrological model**

158   This study used the distributed eco-hydrological model GBEHM (geomorphology-

159   based ecohydrological model), which was developed by Yang et al. (2015) and Gao et

160   al. (2016). The GBEHM is a spatial distributed model for large-scale river basins. It

161   employs geomorphologic properties to reduce the lateral two-dimensions into one-

162   dimension for flow routing within a sub-catchment, which greatly improves the

163   computational efficiency while retaining the spatial heterogeneity in water flow paths

164   at the basin scale. As shown in Figure 2, the GBEHM used a 1-km grid system to

165   discretize the study catchment, which was divided into 251 sub-catchments. Each sub-

166   catchment was further divided into flow-intervals along its main stream. To capture the

167   sub-grid topography, each 1-km grid was represented by a number of hillslopes with an

168   average length and gradient, but different aspect, which were estimated from the 90-m

169   DEM. Additional hillslope properties include soil and vegetation types (Yang et al.,

170   2015).

171   The hillslope is the basic unit in the hydrological simulation of the water and heat

172   transfers (both conduction and convection) in the vegetation canopy, snow/glacier, and

173   soil layers. The canopy interception, radiation transfer in the canopy and the energy

174   balance of the land surface are described using the methods of SIB2 (Sellers et al., 1985,

175   1996). The surface runoff on the hillslope is solved using the kinematic wave equation.

176   The groundwater aquifer is considered as individual storage unit corresponding to each

177   grid. Exchange between the groundwater and the river water is calculated using Darcy's

178   law (Yang et al., 1998, 2002; Cong et al., 2009).

179   The model runs with a time step of 1 hour. Runoff generated from the grid is the

180   lateral inflow into the river over the same flow interval in the corresponding sub-

181   catchment. Flow routing in the river network is calculated using the kinematic wave

182   equation following the sequence determined by the Horton-Strahler scheme (Strahler,

183   1957). The model is driven by the atmosphere forcing data and land surface data

184   introduced in section 2.

185   **3.2 Simulation of cryospheric processes**

186   The simulation of cryospheric processes in the GBEHM includes glacier ablation,

187   snow melting, and soil freezing and thawing.

188   (1) Glacier ablation

189   Glacier ablation is simulated using the following energy balance model (Oerlemans,

190   2001):

191
$$Q_M = SW(1-\alpha) + LW_{in} - LW_{out} - Q_H - Q_L - Q_G + Q_R \qquad (1)$$

192   where Q_M is the net energy absorbed by the surface of the glacier (W·m^{-2}); SW is the

193   incoming shortwave radiation (W·m^{-2}); α is the surface albedo; LW_{in} is the incoming

194   longwave radiation (W·m^{-2}); LW_{out} is the outgoing longwave radiation (W·m^{-2}); Q_H is

195   the sensible heat flux (W·m^{-2}); Q_L is the latent heat flux (W·m^{-2}); Q_R is the energy from

196   rainfall (W·m^{-2}); and Q_G is the penetrating shortwave radiation (W·m^{-2}). The surface

197   albedo is calculated as follows (Oerlemans and Knap, 1998):

$$\alpha = \alpha_{snow} + (\alpha_{ice} - \alpha_{snow})e^{-h/d^*}$$

198   (2)

199   where α_{snow} is the albedo of snow on the glacier surface; α_{ice} is the albedo of the ice

200   surface; h is the snow depth on the glacier surface (m); d^* is a parameter describing the

201   snow depth effect on the albedo (m).

202   The amount of melt water is calculated as (Oerlemans, 2001):

$$M = \frac{Q_M}{L_f}dt$$

203   (3)

204   where dt is the time step used in the model (s) and L_f is the latent heat of fusion (J·kg^{-}

205   ^{1}).

206   (2) Snow melt

207   A multi-layer snow cover model is used to describe the mass and energy balance of

208   snow cover. The snow parametrization is based on Jordan (1991), and two constituents,

209   namely, ice and liquid water, are used to describe each snow layer. For each snow layer,

210   temperature is solved using an energy balance approach (Bartelt and Lehnin, 2002):

211
$$C_s \frac{\partial T_s}{\partial t} - L_f \frac{\partial \rho_i \theta_i}{\partial t} = \frac{\partial}{\partial z}(K_s \frac{\partial T}{\partial z}) + \frac{\partial I_R}{\partial z} + Q_R \qquad (4)$$

212   where C_s is the heat capacity of snow (J·m^{-3}·K^{-1}); T_s is the temperature of the snow

213   layer (K); ρ_i is the density of ice (kg·m^{-3}); θ_i is the volumetric ice content; K_s

214   is the thermal conductivity of snow (W·m^{-1}·K^{-1}); L_f is the latent heat of ice fusion (J·kg^{-}

215   ^{1}) ; I_R is the radiation transferred into the snow layer (W·m^{-2}); and Q_R is the energy

216   delivered by rainfall (W·m^{-2}), which is only considered for the top snow layer. The solar

217   radiation transfer in the snow layers and the snow albedo are simulated using the

218   SNICAR model, which is solved using the method developed by Toon et al. (1989). Eq.

219   (4) is solved using an implicit centered finite difference method, and a Crank-Nicholson

220   scheme is employed.

221   The mass balance of the snow layer is described as follows (Bartelt and Lehnin, 2002):

222 $$\frac{\partial \rho_i \theta_i}{\partial t} + M_{iv} + M_{il} = 0 \qquad (5)$$

223 $$\frac{\partial \rho_l \theta_l}{\partial t} + \frac{\partial U_l}{\partial z} + M_{lv} - M_{il} = 0 \qquad (6)$$

224   where ρ_l is the density of the liquid water (kg·m^{-3}); θ_l is the volumetric liquid water

225   content; U_l is the liquid water flux (kg·m^{-2}·s^{-1}); M_{iv} is the mass of ice that changes into

226   vapour within a time step (kg·m^{-3}·s^{-1}); M_{il} is the mass of ice that changes into liquid

227   water within a time step (kg·m^{-3}·s^{-1}); and M_{lv} is the mass of liquid water that changes

228   into vapour within a time step (kg·m^{-3}·s^{-1}). The liquid water flux of the snow layer is

229   calculated as follows (Jordan, 1991):

230 $$U_l = -\frac{k}{\mu_l} \rho_l^2 g \qquad (7)$$

231   where k is the hydraulic permeability (m^2), μ_l is dynamic viscosity of water at 0 ℃

232   (1.787·10^{-3} N· s·m^{-2}), ρ_l is the density of liquid water (kg·m^{-3}) and g is gravitational

233   acceleration (m·s^{-2}). The water flux of the bottom snow layer is considered snowmelt

234   runoff.

235   (3) Soil freezing and thawing

236   The energy balance of the soil layer is solved as follows (Flerchinger and Saxton,

237   1989):

$$238 \qquad C_s \frac{\partial T}{\partial t} - \rho_i L_f \frac{\partial \theta_i}{\partial t} - \frac{\partial}{\partial z}(\lambda_s \frac{\partial T}{\partial z}) + \rho_l c_l \frac{\partial q_l T}{\partial z} = 0 \qquad (8)$$

239 where C_s is the volumetric soil heat capacity (J·m^{-3}·K^{-1}); T is the temperature (K) of

240 the soil layers; z is the vertical depth of the soil (m); θ_i is the volumetric ice content;

241 ρ_i is the density of ice (kg·m^{-3}); λ_s is the thermal conductivity (W·m^{-1}·K^{-1}); ρ_l is

242 the density of liquid water (kg·m^{-3}); and c_l is the specific heat of liquid water

243 (J·kg^{-1}·K^{-1}). In addition, q_l is the water flux between different soil layers (m·s^{-1}) and is

244 solved using the 1-D vertical Richards equation. The unsaturated soil hydraulic

245 conductivity is calculated using the modified van Genuchten's equation (Wang et al.,

246 2010), as follows:

$$247 \qquad K = f_{ice} K_{sat} (\frac{\theta_l - \theta_r}{\theta_s - \theta_r})^{1/2} [1 - (1 - (\frac{\theta_l - \theta_r}{\theta_s - \theta_r})^{-1/m})^m]^2 \qquad (9)$$

248 where K is the unsaturated soil hydraulic conductivity (m·s^{-1}); K_{sat} is the saturated

249 soil hydraulic conductivity (m·s^{-1}); θ_l is the volumetric liquid water content; θ_s is

250 the saturated water content; θ_r is the residual water content; m is an empirical

251 parameter in van Genuchten's equation and f_{ice} is an empirical hydraulic conductivity

252 reduction factor that is calculated using soil temperature as follows (Wang et al., 2010):

$$253 \qquad f_{ice} = \exp[-10(T_f - T_{soil})], \quad 0.05 \leq fice \leq 1 \qquad (10)$$

254 where T_f is 273.15 K and T_{soil} is the soil temperature.

255 Equation. (8) solves the soil temperature with the upper boundary condition as the

256 heat flux into the uppermost soil layer. When the ground is not covered by snow, the

257 heat flux from the atmosphere into the uppermost soil layer is expressed as follows

258 (Oleson et al., 2010):

$$259 \qquad h = S_g + L_g - H_g - \lambda E_g + Q_R \qquad (11)$$

260   where h is the upper boundary heat flux into the soil layer (W·m^{-2}); S_g is the solar

261   radiation absorbed by the uppermost soil layer (W·m^{-2}); L_g is the net long wave

262   radiation absorbed by the ground (W·m^{-2}), H_g is the sensible heat flux from the ground

263   (W·m^{-2}); λE_g is the latent heat flux from the ground (W·m^{-2}); and Q_R is the energy

264   delivered by rainfall (W·m^{-2}). When the ground is covered by snow, the heat flux into

265   the uppermost soil layer is calculated as follows:

266
$$h = I_p + G \qquad (12)$$

267   where I_p is the radiation that penetrates the snow cover, and G is the heat conduction

268   from the bottom snow layer to the uppermost soil layer. Eq (8) is solved using a finite

269   difference scheme with an hourly time step, similar to the solution of Eq (4).

270   There are no available observations of the geothermal heat flux for the northeastern

271   QTP. To simulate permafrost we assume an upward thermal heat flux at the bottom

272   boundary and estimate its value to be 0.14 W·m^{-2} at a depth of 50 m using the average

273   geothermal gradient from the 4 boreholes (T1-T4) shown in Figure 3, which is

274   reasonable based on a comparison with the observations (0.02 W·m^{-2} to 0.16 W·m^{-2})

275   from the interior of the QTP (Wu et al., 2010). The vertical soil column is divided into

276   39 layers in the model (Figure 2). The 1.7 m topsoil layer is subdivided into 9 layers.

277   The first soil layer at the surface is 0.05 m, and the layer thicknesses increase with depth

278   linearly from 0.05 m to 0.3 m at a depth of 0.8 m. Then thicknesses decrease linearly

279   with depth reaching 0.1 m at a depth of 1.7 m. From 1.7 m to 3.0 m, there are 12 soil

280   layers with a constant thickness of 0.1 m to try to capture the maximum freezing depths

281   according to field observations. From the depth of 3 m to 50 m, there are 18 layers with

282 thicknesses increasing exponentially from 0.1 m to 12 m. The liquid soil moisture, ice

283 content, and soil temperature of each layer is calculated at each time step. The soil heat

284 capacity and soil thermal conductivity are estimated using the method developed by

285 Farouki (1981). Permafrost is defined as ground with a temperature at or below 0 ℃

286 for at least two consecutive years (Woo, 2012). This study differentiated permafrost

287 from seasonally frozen ground based on the simulated vertical ground temperature

288 profile in each grid. For each year in each grid, the frozen ground condition was

289 determined by searching the ground temperature profile within a four-year window

290 from the previous three years to the current year.

291 **3.3 Model calibration**

292 To initialize the model, we first estimated the soil temperature profiles based on the

293 assumption that there is a linear relationship between the ground temperature at a given

294 depth below the surface and elevation. This temperature-elevation relationship is

295 estimated from the observed ground temperatures in 6 boreholes (see Figure 1). Next,

296 the model had a 500-year spin up run to specify the initial values of the hydrological

297 variables (e.g., soil moisture, soil ice content, ground temperature, and groundwater

298 table) by repeating the atmospheric forcing data from 1961 to 1970.

299 This study used the period of 2002 to 2006 for model calibration and the period of

300 2008 to 2012 for model validation. The daily ground temperature at the Qilian station

301 and the frozen depths at the Qilian and Yeniugou stations were used to calibrate the

302 ground surface reflectance according to vegetation type. The other parameters, such as

303 groundwater hydraulic conductivity, were calibrated according to the observed

304 baseflow discharge in the winter season at the Qilian, Zhamashike and Yingluoxia

305 stations. The Nash-Sutcliffe efficiency and relative error are calculated using observed

306 and simulated discharge to evaluate the model performance. We calibrated the surface

307 retention capacity and surface roughness to match the observed flood peaks, and

308 calibrated the leaf reflectance, leaf transmittance and maximum Rubsico capacity of the

309 top leaf based on the remote sensing evapotranspiration data. Table 1 shows the major

310 parameters used in the model.

311   We also simulated the hydrological processes without the frozen soil scheme in order

312 to investigate the impact of frozen soils. In this case, the phase transition of soil water

313 between the solid and the liquid is not considered, although the ground temperature is

314 still simulated. Other processes are simulated in the same manner as in the normal run.

315 **4. Results**

316 **4.1 Validation of the hydrological model**

317   We conducted a comprehensive validation of the GBEHM using the ground

318 temperature profiles observed from six boreholes, the long-term observations of ground

319 temperature and frozen depths from the Qilian and Zhamashike stations, the soil

320 moisture observations from the A'rou Sunny Slope station, the long-term observations

321 of streamflow from the three hydrological stations shown in Figure 1 and the monthly

322 actual evapotranspiration estimated from remote sensing data.

323   Figure 3 shows the comparison of the model-simulated and observed ground

324 temperature profiles at the six boreholes. The model generally captured the vertical

325 distribution of the ground temperature at T1, T2, T3 and T4 in the permafrost area, but

326   the temperatures were overestimated above 20 m depth for T1 and T3. Good agreement

327   between the simulated and observed ground temperature profiles below the depth of 20

328   m is probably due to fitting of initial values. Therefore, the deep ground temperatures

329   are stable, which is confirmed by the comparison of temperature profiles in different

330   years, as shown in Figure S1 in the supplementary material. Figure S1 also illustrates

331   that the temperatures above 20 m have shown significant increasing trends over the past

332   40 years. The errors in simulating the vertical temperature profile near the surface might

333   be caused by simplification of the 3-D topography. At T5, which is located in seasonally

334   frozen ground, the simulated ground temperature profile did not agree well with the

335   observed profile at depths of 4-20 m. This error might also be related to heterogeneity

336   in the ground properties, especially the thermal conductivity and heat capacity, since no

337   such information was available. The model simulation agrees well with the borehole

338   observations at T7, which is located in the transition zone from permafrost to seasonally

339   frozen ground. Therefore, the model can identify the boundary between the permafrost

340   and seasonally frozen ground.

341   We also validated the model simulation of the freezing/thawing cycles based on long-

342   term observations of ground temperature and frozen depth. Figure 4 compares the

343   simulated ground temperature with the observed temperature at the Qilian station,

344   which is located in seasonally frozen ground (observed daily ground temperature data

345   are available from 2004). Generally, the model simulations accurately captured the

346   seasonal changes in the ground temperature profile. Validation of the ground

347   temperature at different depths (0.05 m, 0.1 m, 0.2 m, 0.4 m, 0.8 m, 0.16 m, and 0.32

348 m) showed that the root mean square error (RMSE) decreases with increasing depth.

349 The RMSE was approximately 2.5 ℃ for the uppermost three depths (0.5 m, 0.10 m

350 and 0.2 m). The RMSE for depths of 0.4 cm and 0.8 m were 1.7 ℃ and 1.5 ℃,

351 respectively, and the RMSE for a depth of 3.2 m was 0.9 ℃. Uncertainties in the

352 simulations may be related to the ground heat capacity and thermal conductivity

353 estimated according to Farouki (1981), and the results are similar to the findings by Ou

354 et al. (2016) using the Northern Ecosystem Soil Temperature (NEST) model. We

355 compared the model-simulated daily frozen depth with in situ observations at the Qilian

356 and Yeniugou stations from 2002 to 2014, as shown in Figure 5. The model reproduced

357 well the daily variations in frozen depth, although the depth was underestimated by

358 approximately 0.5 m at the Yeniugou station. In general, the validation of ground

359 temperature and frozen depth indicates that the model effectively captured the freezing

360 and thawing processes in the upper Heihe basin.

361 Furthermore, we used the the observed hourly liquid soil moisture at the A'rou Sunny

362 Slope station for an additional independent validation. Figure S2 in the supplementary

363 material shows the comparison between the simulated and observed liquid soil moisture

364 at different depths from January 1 to December 31, 2014. This comparison

365 demonstrates that the model simulation of liquid soil moisture is reasonable.

366 Figure 6 compares the model simulated and the observed daily streamflow discharge

367 at the Yingluoxia, Qilian and Zhamashike stations. The model simulations agreed well

368 with the observations. The model simulations captured the flood peaks and the

369 magnitude of base flow in both the calibration and validation periods. For the

370 Yingluoxia, Qilian and Zhamashike stations, the Nash-Sutcliffe efficiency (NSE)

371 coefficients were 0.64, 0.63 and 0.72, respectively, in the calibration period and 0.64,

372 0.60, and 0.73, respectively, in the validation period. The relative error (RE) was within

373 10% for both the calibration and validation periods (Figure 6). Figure S3 in the

374 supplementary material shows the comparison of the model-simulated monthly actual

375 evaporation data and the remote sensing-based evaporation data for the entire

376 calibration and validation periods. The GBEHM simulation showed similar temporal

377 variations in actual evapotranspiration compared with the remote sensing based

378 estimation, and the RMSE of the simulated monthly evapotranspiration was 9.1 mm in

379 the calibration period and 7.1 mm in the validation period.

380 We also compared the model-simulated river discharges with and without the frozen

381 soil scheme. Table S1 in the supplementary material shows that the model with the

382 frozen soil scheme achieves a better simulation of the daily hydrograph than the model

383 without the frozen soil scheme. Figure S4 in the supplementary material shows that the

384 model without the frozen soil scheme overestimates the river discharge in the freezing

385 season and underestimates flood peaks in the warming season.

386 **4.2 Long-term changes in frozen soils**

387 In the upper Heihe basin, the ground surface starts to freeze in November and begins

388 to thaw in April (Wang et al., 2015a). From November to March, the ground surface

389 temperature is below 0℃ in both the permafrost and seasonally frozen ground regions,

390 and precipitation mainly falls in the period from April to October. Therefore, to

391 investigate the changes in frozen soils and their hydrological impact, a year is

392   subdivided into two seasons, i.e., the freezing season (November to March) and the

393   thawing season (April to October). Increasing precipitation and air temperature in the

394   study area in both seasons over the past 50 years were reported in a previous study

395   (Wang et al., 2015b). Compared to the decadal mean for 1971 to 1980, the annual mean

396   air temperature for the 2001 to 2010 period was approximately 1.2 ℃ higher, with a

397   larger increase in the freezing season (1.4 ℃) than in the thawing season (1.1 ℃)

398   (Table S2).

399   Figure 7 shows the changes in the basin-averaged ground temperature in the freezing

400   and thawing seasons. The ground temperature increased in all seasons, especially over

401   the past 30 years. The increasing trend of ground temperature was larger in the freezing

402   season than in the thawing season. In the freezing season (Figure 7(a)), the top layer

403   ground temperature was lower than the deep layer temperature. The linear trend of the

404   top layer (0-0.5 m) ground temperature was 0.49 ℃·decade^{-1} and the trend of the deep

405   layer (2.5-3 m) temperature was 0.32 ℃·decade^{-1}. The ground temperature in the deep

406   layer (2.5-3 m) changed from -0.7 ℃ in the 1970s to approximately 0 ℃ in the most

407   recent decade. In the thawing season (Figure 7(b)), the increasing trend of the top layer

408   (0-0.5 m) ground temperature (0.29 ℃·decade^{-1}) was greater than that of the deep layer

409   (2.5-3 m) temperature (0.22 ℃·decade^{-1}). The warming trend was larger in shallow

410   ground layers; this is because the surface heat flux is impeded by the thermal inertia as

411   it penetrates to greater depths.

412   Figure 8 shows the change in permafrost area during 1971-2013. As shown in Figure

413   8(a), the permafrost areas decreased by approximately 8.8% (from 5700 km^2 in the

414   1970s to 5200 km^2 in the 2000s), indicating an evident decrease in the permafrost extent

415   in the upper Heihe basin in the past 40 years.

416   Figure 8 (b) shows the changes in the basin-averaged maximum frozen depth in the

417   seasonally frozen ground areas and active layer thickness in the permafrost areas. The

418   basin-averaged annual maximum frozen depth showed a significant decreasing trend

419   (0.032 m·decade^{-1}). In addition, the maximum frozen depth had a significantly negative

420   correlation with the annual mean air temperature (r = -0.71). Simulated active layer

421   thickness in the permafrost regions increased (0.043 m·decade^{-1}), and correlated

422   positively with the annual mean air temperature (p = 0.005).

423   Figure 9 shows the frozen soil distributions in the periods of 1971 to 1980 and 2001

424   to 2010. Comparing the frozen soil distributions of the two periods, we observed major

425   changes in the frozen soils on sunny slopes at elevations between 3500 and 3900 m,

426   especially in the west tributary, where large areas of permafrost changed into seasonally

427   frozen ground. Figure S5, illustrating the taliks simulated in the period of 2001-2010,

428   shows that taliks were mainly located on the edge of the permafrost area and that talik

429   development was not significant.

430   Figure 10 shows the monthly mean ground temperatures for areas with elevations

431   between 3300 and 3500 m and over areas with elevations between 3500 and 3700 m in

432   the upper Heihe basin. In the areas with elevations between 3300 and 3500 m located

433   in the seasonally frozen ground region (Figure 10(a)), the frozen depth decreased and

434   the ground temperature in deep layers (depths greater than 2 m) increased. Figure 10(b)

435   shows that the increase in ground temperature was larger in the area with higher

436 elevation (3500-3700 m). This figure shows that the thickness of the permafrost layer

437 decreased as the ground temperature increased, and the permafrost changed into

438 seasonally frozen ground after 2000. The surface thaw depths changed slowly

439 compared with the depth to the base of permafrost as shown in Figure 10, which may

440 be primarily due to the geothermal heat flux. Additionally, the faster increase in the air

441 temperature in the freezing season (0.41 ℃ decade^{-1}) than in the thawing season

442 (0.26 ℃ decade^{-1}) may be another reason.

443 **4.3 Changes in the water balance and runoff**

444   Table 2 shows the decadal changes in the annual water balance from 1971 to 2010

445 based on the model simulation. The annual precipitation, annual runoff and annual

446 runoff ratio exhibited the same decadal variation; however the annual

447 evapotranspiration maintained an increasing trend starting in the 1970s that was

448 consistent with the rising air temperature and soil warming. Although the actual

449 evapotranspiration increased, the runoff ratio remained stable during the past 4 decades

450 because of the increased precipitation.

451   Figure 11 and Table 2 show the changes in runoff (both simulated and observed) in

452 different seasons. The model-simulated and observed runoff both exhibited significant

453 increasing trends in the freezing season and in the thawing season. Therefore, the model

454 simulation effectively reproduced the observed long-term changes. In the freezing

455 season, since there was no glacier or snow melting (see Table 2), the runoff was mainly

456 subsurface flow (groundwater flow and lateral flow from the unsaturated zone). In the

457 thawing season, as shown in Table 2, snowmelt runoff contributed approximately 14%

458   of the total runoff, whereas glacier runoff contributed only a small fraction of the total

459   runoff (approximately 2.2%). Rainfall runoff was the major component of the total

460   runoff in the thawing season, and the runoff increase in the thawing season was mainly

461   due to increased precipitation and snowmelt. As shown in Figure 11, the actual

462   evapotranspiration increased significantly in both seasons due to increased precipitation

463   and ground warming. The increase in actual evapotranspiration was greater in the

464   thawing season than in the freezing season.

465   Figure 12 shows the changes in the basin-averaged annual liquid soil water storage

466   (0-3 m) and groundwater storage. The annual liquid soil water storage showed a

467   significant increasing trend, especially in the most recent 3 decades. This long-term

468   change in liquid water storage was similar to the runoff change in the freezing season,

469   as shown in Figure 11 (a), exhibiting a correlation coefficient of 0.79. The annual ice

470   water storage in the top 0-3 m soil layers showed a significant decreasing trend due to

471   frozen soil changes. Annual groundwater storage showed a significantly increasing

472   trend especially in the most recent 3 decades, which indicates that the groundwater

473   recharge has increased with permafrost degradation.

474   **5.   Discussion**

475   **5.1 Impact of frozen soil changes on the soil moisture and runoff**

476   We have plotted the long-term changes in the spatially averaged liquid soil moistures

477   in the areas with elevations between 3300 and 3500 m and in the areas with elevations

478   between 3500 and 3700 m in Figure S6 in the supplementary material. In the seasonally

479   frozen ground at elevations of 3300-3500 m, the liquid soil moisture increased slightly

480   due to the decrease in the frozen depth (Figure 10(a)). At elevations of 3500-3700 m,

481   the liquid soil moisture in the deep layer increased significantly since the 1990s, due to

482   the change of the permafrost into seasonally frozen ground (Figure 10 (b)).

483   In the freezing season, since the surface ground is frozen, runoff is mainly subsurface

484   flow coming from seasonally frozen ground. Runoff has the highest correlation (r =

485   0.82) with the liquid soil moisture in the freezing season, which indicates that the frozen

486   soil changes were the primary cause of the increase in liquid soil moisture, resulting in

487   increased runoff in the freezing season. During the past 40 years, parts of permafrost

488   changed into seasonally frozen ground and the frozen depth of the seasonally frozen

489   ground decreased, leading to increases in the liquid soil moisture in the deep layers

490   during the freezing season. The increase in liquid soil moisture also increased the

491   hydraulic conductivity, which enhanced the subsurface flow. Figure 13(c) shows the

492   seasonal pattern of runoff from the entire basin. From April to October (the thawing

493   season), runoff in the permafrost area was much larger than in the area of seasonally

494   frozen ground; however, in the freezing season the inverse was true. Figure S7 in the

495   supplementary material shows runoff changes from a typical area (with elevations of

496   3500-3700 m) that featured permafrost during the period of 1971 to 1980, but degraded

497   to seasonally frozen ground during the period of 2001 to 2010. This illustrates that

498   thawing of permafrost increased runoff in the freezing season and slowed hydrological

499   recession processes in autumn. Figure S4 illustrates the increase in freezing season

500   runoff and the shift in the seasonal flow patterns simulated by the model without the

501   frozen soil scheme.

502   Figure 13 shows the large difference in runoff variation with elevation between the

503   freezing and thawing seasons. In the freezing season, the runoff change from the 1970s

504   to the 2000s in the areas of seasonally frozen ground (mainly located below 3500 m,

505   see Figure 9) was relatively small. The areas with elevations of 3500-3900 m showed

506   large changes in runoff. This pattern is due to the shift from permafrost to seasonally

507   frozen ground in some areas in the elevation range of 3500 to 3900 m, as simulated by

508   the model, particularly for sunny hillslopes (see Figure 9). This finding illustrates that

509   a change from permafrost to seasonally frozen ground has a larger impact on the runoff

510   than a change in frozen depth in areas of seasonally frozen ground. In the thawing

511   season, runoff increased with elevation due to the increase in precipitation with

512   increasing elevation, and the magnitude of the runoff increase was mainly determined

513   by magnitude of the precipitation increase (Gao et al., 2016). Precipitation in the region

514   with elevations below 3100 m was low, and the air temperature was high. Hence, runoff

515   in this region was lower during 2001-2010 than during 1971-1980 because of greater

516   evapotranspiration.

517   **5.2 Comparison with the previous similar studies**

518   In this study, the model simulation showed that the thawing of frozen soils led to

519   increased freezing season runoff and base flow in the upper Heihe basin. This result is

520   consistent with previous findings based on observations in high latitude regions

521   (Walvoord and Striegl, 2007; Jacques and Sauchyn, 2009; Ye et al., 2009) and in

522   northeast China (Liu et al., 2003). However, those studies did not consider spatial

523   variability. This study found that the impact of the frozen soil thawing on runoff varied

524   regionally. In the upper Heihe basin (see Figure 13), the change in the freezing season

525   runoff was strongly affected by the change from permafrost to seasonally frozen ground

526   in the higher-elevation region and by the evaporation increase in the lower-elevation

527   region due to rising air temperature. However, runoff at the basin scale mainly came

528   from the higher-elevation regions.

529   This study also showed that the thawing of frozen soils increased the liquid soil

530   moisture in the upper Heihe basin, which is consistent with the finding of Subin et al.

531   (2013) using the CLM model to simulate northern high-latitude permafrost regions, and

532   the findings of Cuo et al. (2015) using the VIC model to simulate 13 sites on the QTP.

533   In contrast, Lawrence et al. (2015) found that permafrost thawing reduced soil moisture

534   based on CLM model simulations of the global permafrost region. This finding might

535   be related to the uncertainties in the soil water parameters and the high spatial

536   heterogeneity of soil properties, which are difficult to consider in a global-scale model.

537   Subin et al. (2013) and Lawrence et al. (2015) simulated the soil moisture changes in

538   the active layer of permafrost over large areas with coarse spatial resolution. Unlike

539   those studies, this study investigated the spatio-temporal variability in soil moisture

540   using a high spatial resolution and analyzed the impacts of frozen soil changes.

541   Jin et al. (2009) found decreased soil moisture and runoff due to permafrost

542   degradation based on observations at the plot scale in the source area of the Yellow

543   River basin. These results are different from those in the present study, possibly due to

544   the difference in the hydrogeological structure and soil hydraulic parameters between

545   the source area of the Yellow River and the upper Heihe basin. Wang et al. (2015a)

546   estimated the increasing trend of the maximum frozen depth in the seasonally frozen

547   ground to be 0.04 m·decade^{-1} during 1972-2006 in the Heihe River basin based on plot

548   observations, which is consistent with the results in this study. The increase in

549   groundwater storage illustrated in this study is also consistent with the findings of Cao

550   et al. (2012) based on GRACE data, which showed that groundwater storage increased

551   during the period of 2003~2008 in the upper Heihe basin.

552   **5.3 Uncertainty in simulation of the frozen soils**

553   Estimation of the change in permafrost area is a great challenge due to such complex

554   factors as climatology, vegetation, and geology. Guo et al. (2013) reported that the

555   permafrost area for the whole QTP decreased from approximately 175.0×10^4 km^2 in

556   1981 to 151.5×10^4 km^2 in 2010, with a relative change of 13.4%. Wu et al. (2005)

557   reported that the permafrost area decreased by 12% from 1975 to 2002 in the Xidatan

558   basin of the QTP based on a ground penetration radar survey. Jin et al. (2006) found an

559   area reduction of 35.6% in island permafrost in Liangdaohe, which is located along the

560   southern portion of the Qinghai-Tibet Highway, from 1975 to 1996. Compared with the

561   borehole observations by Wang et al. (2013) shown in Figure 2, our model slightly

562   overestimated the soil temperature in permafrost areas, possibly leading to an

563   overestimation of the rate of permafrost area reduction.

564   There were two major uncertainties in the frozen soils simulation: uncertainty in the

565   simulation of the land surface energy balance and uncertainty in the simulation of the

566   soil heat-water transfer processes (Wu et al., 2016). Uncertainty in the land surface

567   energy balance simulation might result from uncertainty in the radiation and surface

568   albedo estimates due to the complex topography, vegetation cover and soil moisture

569   distribution, thereby introducing uncertainties into the estimated ground temperature

570   and soil heat flux. The uncertainty in the simulation of soil heat-water transfer processes

571   might result from the soil water and heat parameters and the bottom boundary

572   conditions of heat flux. For example, the soil depth and the fraction of rock in soil can

573   greatly affect the ground temperature simulation. Permafrost degradation is closely

574   related to the thermal properties of rocks and soils, the geothermal flow and the initial

575   ground temperature and soil ice conditions. Sub-grid topography may also affect the

576   frozen soil simulation. For example, active layer thickness is different between the low-

577   elevation valleys and higher-elevation slopes due to the temperature inversion caused

578   by the accumulation of cold air in valleys (Bonnaventure et al., 2012; Zhang et al., 2013;

579   O'Neill et al., 2015). In areas with high groundwater flow rates, laterally advected heat

580   flux may increase the thawing of permafrost (Kurylyk et al., 2016; Sjöberg et al., 2016).

581   Not considering the lateral heat flux may lead to an underestimation of talik

582   development and thawing rates of permafrost. In addition, uncertainties in the input

583   data, particularly solar radiation (which is estimated using interpolated sunshine hour

584   data from a limited number of observational stations) and precipitation (which is also

585   interpolated based on observations at these stations), may also influence the results of

586   the model simulation. Due to the complexity of the distributed model and the large

587   number of model parameters, quantifying the overall simulation uncertainty is

588   challenging, but is part of our ongoing research.

589   **6. Conclusions**

590 This work carefully validated a distributed hydrological model coupled with

591 cryospheric processes in the upper Heihe River basin using available observations of

592 soil moisture, soil temperature, frozen depth, actual evaporation and streamflow

593 discharge. Based on the model simulations from 1971 to 2013 in the upper Heihe River,

594 the long-term changes in frozen soils were investigated, and the effects of the frozen

595 soil changes on the hydrological processes were explored. Based on these analyses, we

596 have reached the following conclusions:

597 (1) The model simulation suggests that 8.8% of the permafrost areas degraded into

598 seasonally frozen ground in the upper Heihe River basin during 1971-2013,

599 predominantly between elevations of 3500 m and 3900 m. The results indicate that the

600 decreasing trend of the annual maximum frozen depth of the seasonally frozen ground

601 is 0.032 m·decade^{-1}, which is consistent with previous observation-based studies at the

602 plot scale. Additionally, our work indicates a trend of increasing active layer thickness

603 in the permafrost regions of 0.043 m·decade^{-1}.

604 (2) The model-simulated runoff trends agree with the observed trends. In the freezing

605 season (November-March), based on the model simulation, runoff was mainly sourced

606 from subsurface flow, which increased significantly in the higher elevation regions

607 where significant frozen soil changes occurred. This finding implies that the runoff

608 increase in the freezing season is primarily caused by frozen soil changes (permafrost

609 degradation and reduced seasonally frozen depth). In the thawing season (April-

610 October), the model simulation indicates that runoff was mainly sourced from rainfall

611 and showed an increasing trend at higher elevations, which can be explained by the

612 increase in precipitation. In both the freezing and thawing seasons, the model-simulated

613 runoff decreased in the lower-elevation regions, which can be explained by increased

614 evaporation due to rising air temperatures.

615   (3) The model-simulated changes in soil moisture and ground temperature indicate

616 that the annual storage of liquid water increased, especially in the most recent three

617 decades, due to frozen soil changes. The annual ice water storage in the top 0-3 m of

618 soil showed a significant decreasing trend due to soil warming. The model simulated

619 annual groundwater storage had an increasing trend, which is consistent with the

620 changes observed by the GRACE satellite. Therefore, groundwater recharge in the

621 upper Heihe basin has increased in recent decades.

622   (4) The model simulation indicated that regions where permafrost changed into

623 seasonally frozen ground had larger changes in runoff and soil moisture than the areas

624 covered by seasonally frozen ground throughout the study period.

625   For a better understanding of the changes in frozen soils and their impact on

626 ecohydrology, the interactions among soil freezing-thawing processes, vegetation

627 dynamics and hydrological processes need to be investigated in future studies. There

628 are uncertainties in simulations of frozen soils and hydrological processes that also

629 warrant further investigation.

630

631 **Acknowledgements:** This research was supported by the major plan of "Integrated

632 Research on the Ecohydrological Processes of the Heihe Basin" (Project Nos.

633 91225302 and 91425303) funded by the National Natural Science Foundation of China

634 (NSFC). The authors would like to thank the editor and reviewers for their constructive

635 suggestions, which have substantially improved the paper. All data cited in this paper

636 are available from the references. The model code with a working example is freely

637 available from our website (https://github.com/gb03/GBEHM) or upon request from

638 the corresponding author (yangdw@tsinghua.edu.cn).

639

640 **References**

641 Bartelt P. and M. Lehning: A physical snowpack model for the swiss avalanche warning: PartⅠ:

642   numerical model, Cold Regions Sci. and Tech., 35(3), 123-145, doi: 10.1016/S0165-

643   232X(02)00074-5, 2002.

644 Bonnaventure PP, Lewkowicz AG, Kremer M, Sawada MC: A Permafrost Probability Model for the

645   Southern Yukon and Northern British Columbia, Canada, Permafrost and Periglac. Process., 23,52-

646   68, doi: 10.1002/ppp.1733, 2012.

647 Cao Y., Nan Z. and Hu X.: Estimating groundwater storage changes in the Heihe river basin using

648   GRACE, in: IEEE International Geoscience and Remote Sensing Symposium (IGARSS), Munich,

649   Germany, 22–27 July 2012, 798-801, 2012.

650 Chen, R., Lu, S., Kang, E., Ji, X., Zhang, Z., Yang, Y., Qing, W.: A distributed water-heat coupled model

651   for mountainous watershed of an inland river basin of Northwest China (I) model structure and

652   equations, Environ. Geol., 53, 1299-1309, doi: 10.1007/s00254-007-0738-2,2008.

653 Cheng, G. and Jin, H.: Permafrost and groundwater on the Qinghai-Tibet Plateau and in northeast China,

654   Hydrogeol. J., 21, 5-23, doi: 10.1007/s10040-012-0927-2, 2013.

655 Cheng, G., Li, X., Zhao, W., Xu, Z., Feng, Q., Xiao, S., Xiao, H.: Integrated study of the water-

656   ecosystem-economy in the Heihe River Basin. Nat. Sci. Rev., 1(3), 413-428, doi:

657   10.1093/nsr/nwu017, 2014.

658   Cheng, G., and Wu T.: Responses of permafrost to climate change and their environmental significance,

659   Qinghai-Tibet Plateau, J. Geophys. Res., 112, F02S03, doi:10.1029/2006JF000631, 2007.

660   Cherkauer, K. A., and D. P. Lettenmaier: Hydrologic effects of frozen soils in the upper Mississippi River

661   basin, J. Geophys. Res., 104, 19,599-19,610, doi: 10.1029/1999JD900337, 1999.

662   Cong Z T, Yang D W, Gao B, et al.: Hydrological trend analysis in the Yellow River basin using a

663   distributed hydrological model, Water Resour Res, 45: W00A13, doi: 10.1029/2008WR006852,

664   2009.

665   Cuo, L., Y. Zhang, F. Zhu, and L. Liang.: Characteristics and changes of streamflow on the Tibetan

666   Plateau: A review, J. Hydrol.: Reg. Stud., 2, 49-68, doi: 10.1016/j.ejrh.2014.08.004, 2014.

667   Cuo, L., Y. Zhang, T. J. Bohn, L. Zhao, J. Li, Q. Liu, and B. Zhou: Frozen soil degradation and its effects

668   on surface hydrology in the northern Tibetan Plateau, J. Geophys. Res. Atmos., 120,

669   doi:10.1002/2015JD023193, 2015.

670   Duan L., Man X., Kurylyk B. L. and Cai T.: Increasing winter baseflow in response to permafrost thaw

671   and precipitation regime shifts in northeastern China, Water, 9(1), 25, doi:10.3390/w9010025, 2017.

672   Endrizzi S, Gruber S, Dall'Amico M, and R. Rigon: GEOtop 2.0: simulating the combined energy and

673   water balance at and below the land surface accounting for soil freezing, snow cover and terrain

674   effects, Geosci. Model Dev., 7: 2831-2857, doi:10.5194/gmd-7-2831-2014, 2014.

675   Fan, W.: Heihe 1km LAI production, Heihe Plan Science Data Center at Lanzhou,

676   doi:10.3972/heihe.090.2014.db, 2014.

677   Farouki, O.T.: The thermal properties of soils in cold regions, Cold Regions Sci.and Tech., 5, 67-75, doi:

678   10.1016/0165-232X(81)90041-0, 1981.

679   Flerchinger G., Saxton K.: Simultaneous heat and water model of a freezing snow-residue-soil system I.

680   Theory and development, Trans. ASAE, 32, 565-571, doi: 10.13031/2013.31040, 1989.

681   Gao B., Qin Y., Wang YH, Yang DW, and Zheng YR: Modeling Ecohydrological Processes and Spatial

682   Patterns in the Upper Heihe Basin in China, Forests, 7(1),10, doi:10.3390/f7010010, 2016.

683   Guo, D., and H. Wang: Simulation of permafrost and seasonally frozen ground conditions on the Tibetan

684   Plateau, 1981–2010, J. Geophys. Res. Atmos., 118, 5216-5230, doi:10.1002/jgrd.50457, 2013.

685   Hinzman, L.D., C.J. Deal, A.D. McGuire, S.H. Mernild, I.V. Polyakov, and J.E. Walsh: Trajectory of

686   the Arctic as an integrated system, Ecol. Appl., 23(8),1837-1868, doi:10.1890/11-1498.1, 2013.

687   Jacques St., J.-M., and Sauchyn D. J.: Increasing winter baseflow and mean annual streamflow from

688   possible permafrost thawing in the Northwest Territories, Canada, Geophys. Res. Lett., 36, L01401,

689   doi:10.1029/2008GL035822, 2009.

690   Jarvis, A., Reuter, H.I., Nelson, A., Guevara, E.: Hole-filled seamless SRTM data, Version 4,

691   International Centre for Tropical Agriculture (CIAT), 2008.

692   Jin, H., He, R., Cheng, G., Wu, Q., Wang, S., Lu, L. and Chang X.: Changes in frozen ground in the

693   Source Area of the Yellow River on the Qinghai–Tibet Plateau, China, and their eco-environmental

694   impacts, Environ. Res. Lett., 4(4), 045206, doi:10.1088/1748-9326/4/4/045206, 2009.

695   Jin, H.J., Zhao, L., Wang, S.L., Jin, R.: Thermal regimes and degradation modes of permafrost along

696   the Qinghai–Tibet Highway, Science in China D: Earth Sciences, 49 (11), 1170-1183, 2006.

697   Jordan R.: A one-dimensional temperature model for a snow cover, Technical Documentation for

698   SNTHERM.89, Cold Regions Research and Engineering Lab, Hanover NH, 49 pp., 1991.

699   Kurylyk, B. L., M. Hayashi, W. L. Quinton, J. M. McKenzie, and C. I. Voss: Influence of vertical and

700   lateral heat transfer on permafrost thaw, peatland landscape transition, and groundwater flow, Water

701   Resour. Res., 52, 1286-1305, doi:10.1002/2015WR018057, 2016.

702 Lawrence, D.M., C.D. Koven, S.C. Swenson, W.J. Riley, and A.G. Slater: Permafrost thaw and resulting

703   soil moisture changes regulate projected high-latitude CO_2 and CH_4 emissions, Environ. Res. Lett.,

704   10, doi:10.1088/1748-9326/10/9/094011, 2015.

705 Li, D.L., Zhong, H.L., Wu, Q.B., Zhang, Y.J., Hou, Y.L., Tang, M.C.: Analyses on changes of surface

706   temperature over Qinghai–Xizang Plateau, Plateau Meteorology, 24, 291-298, 2005 (in Chinese).

707 Li, X., Cheng, G.D., Liu, S.M., Xiao, Q., Ma, M.G., Jin, R., Che, T., Liu, Q.H., Wang, W.Z., Qi, Y., Wen,

708   J.G., Li, H.Y., Zhu, G.F., Guo, J.W., Ran, Y.H., Wang, S.G., Zhu, Z.L., Zhou, J., Hu, X.L., Xu, Z.W.:

709   Heihe Watershed Allied Telemetry Experimental Research (HiWATER): Scientific Objectives and

710   Experimental Design, B. Am. Meteorol. Soc., 94(8), 1145-1160, doi: 10.1175/BAMS-D-12-00154.1,

711   2013.

712 Liu, X. and Chen, B.: Climate warming in the Tibetan Plateau during recent decades, Int. J. Climatol.,

713   20(1), 1729-1742, doi: 10.1002/1097-0088(20001130)20:14<1729::AID-JOC556>3.0.CO;2-, 2000.

714 Liu, S., Xu Z., Wang W., Bai J., Jia Z., Zhu M., and Wang J.: A comparison of eddy-covariance and large

715   aperture scintillometer measurements with respect to the energy balance closure problem, Hydrol.

716   Earth Syst. Sc., 15(4), 1291-1306, doi:10.5194/hess-15-1291-2011, 2011.

717 Liu J., N. Hayakawab, Lu M., Dong S., and Yuan J.: Hydrological and geocryological response of winter

718   streamflow to climate warming in Northeast China, Cold Regions Sci.and Tech., 37,15-24, doi:

719   10.1016/S0165-232X(03)00012-0, 2003.

720 Wu T., Li S., Cheng G. and N Z.: Using ground-penetrating radar to detect permafrost degradation in

721   the northern limit of permafrost on the Tibetan Plateau, Cold Regions Sci.and Tech., 41, 211-219,

722   2005, doi:10.1016/j.coldregions.2004.10.006.

Niu L., Ye B., Li J., and Sheng Y.: Effect of permafrost degradation on hydrological processes in typical basins with various permafrost coverage in Western China, China Earth Sci., 54(4), 615-624, doi: 10.1007/s11430-010-4073-1, 2011.

Oerlemans, J. and Knap, W.H.: A 1 year record of global radiation and albedo in the ablation zone of Morteratschgletscher, Switzerland, J. Glaciol., 44, 231-238, doi: 10.3198/1998JoG44-147-231-238, 1998.

Oerlemans, J.: Glaciers and Climate Change, Lisse: Swets & Zeitlinger, 2001.

Oleson, K.W., Lawrence, D.M., Bonan, G.B., Flanner, M.G., Kluzek, E., Lawrence, P.J., Levis, S., Swenson, S.C., Thornton, P.E., Dai, A., Decker, M., Dickinson, R., Feddema, J., Heald, C.L., Hoffman, F., Lamarque, J., Mahowald, N., Niu, G., Qian, T., Randerson, J., Running, S., Sakaguchi, K., Slater, A., Stöckli, R., Wang, A., Yang, Z., Zeng, X., Zeng, X.: Technical Description of version 4.0 of the Community Land Model (CLM), NCAR Technical Note NCAR/TN-47+STR, National Center for Atmospheric Research, Boulder, CO, 257 pp., 2010.

Qiu J.: Thawing permafrost reduces river runoff, Nature, doi:10.1038/nature.2012.9749, 2012.

Ou, C., B. Leblon, Y. Zhang, A. LaRocque, K. Webster, and J. McLaughlin: Modelling and mapping permafrost at high spatial resolution using Landsat and RADARSAT images in northern Ontario, Canada: Part 1 - Model calibration, International Journal of Remote Sensing, doi: 10.1080/01431161.2016.1157642, 2016.

O'Neill, H. B., Burn, C. R., Kokelj, S. V. & Lantz, T. C.: 'Warm' tundra: atmospheric and near-surface ground temperature inversions across an alpine treeline in continuous permafrost, western arctic, Canada. Permafrost and Periglac. Process. 26, 103–118, doi: 10.1002/ppp.1838., 2015.

Rawlins M., Lammers R., Frolking S., Fekete B. and Vorosmarty C.: Simulating pan-Arctic runoff with a macro-scale terrestrial water balance model, Hydrol. Process., 17, 2521-2539, doi: 10.1002/hyp.1271, 2003.

747 Rawlins, M.A., D.J. Nicolsky, K.C. McDonald, and V.E. Romanovsky: Simulating soil freeze/thaw

748  dynamics with an improved pan-Arctic water balance model, J. Adv. Model. Earth Syst., 5:659-675,

749  doi:10.1002/jame.20045, 2013.

750 Rigon R., Bertoldi G., and Over TM: GEOtop: A distributed hydrological model with coupled water

751  and energy budgets, J. Hydrometeorol., 7, 371–388, doi: 10.1175/JHM497.1, 2006.

752 Schuur, E.A.G., A.D. McGuire, C. Schädel, G. Grosse, J.W. Harden, D.J. Hayes, G. Hugelinus, C.D.

753  Koven, P. Kuhry, D.M. Lawrence, S.M. Natali, D. Olefeldt, V.E. Romanovsky, K. Schaefer, M.R.

754  Turetsky, C.C. Treat, and J.E. Vonk: Climate change and the permafrost carbon feedback, Nature

755  520,171-179 doi:10.1038/nature14338, 2015.

756 Sellers, P.J.: Canopy reflectance, photosynthesis, and transpiration, Int. J. Remote Sens., 8, 1335-1372,

757  doi: 10.1080/01431168508948283, 1985.

758 Sellers, P.J.; Randall, D.A.; Collatz, G.J.; Berry, J.A.; Field, C.B.; Dazlich, D.A.; Zhang, C.; Collelo,

759  G.D.; Bounoua, L.: A Revised Land Surface Parameterization (SiB2) for Atmospheric GCMS.

760  Part I: Model Formulation, J. Clim., 9, 676-705, doi: 10.1175/1520-

761  0442(1996)009<0676:ARLSPF>2.0.CO;2, 1996.

762 Sjöberg, Y., E. Coon, A. B. K. Sannel, R. Pannetier, D. Harp, A. Frampton, S. L. Painter, and S. W. Lyon:

763  Thermal effects of groundwater flow through subarctic fens: A case study based on field

764  observations and numerical modeling, Water Resour. Res., 52, 1591-1606,

765  doi:10.1002/2015WR017571, 2016.

766 Song X., Brus DJ, Liu F., Li D., Zhao Y., Yang J. and Zhang G.: Mapping soil organic carbon content by

767  geographically weighted regression: A case study in the Heihe River Basin, China, Geoderma,

768  261,11–22, doi: 10.1016/j.geoderma.2015.06.024, 2016.

769   Strahler A N: Quantitative analysis of watershed geomorphology, Eos, Transactions American

770   Geophysical Union, 38(6), 913-920, doi: 10.1029/TR038i006p00913, 1957.

771   Subin Z.M., Koven C.D., Riley W.J., Torn M.S., Lawrence D.M. and Swenson S.C.: Effects of Soil

772   Moisture on the Responses of Soil Temperatures to Climate Change in Cold Regions, J. Clim.,

773   26,3139-3158, doi: 10.1175/JCLI-D-12-00305.1, 2013.

774   Toon, O.B., McKay, C.P., Ackerman, T.P., and Santhanam, K.: Rapid calculation of radiative heating

775   rates and photodissociation rates in inhomogeneous multiple scattering atmospheres, J. Geophys.

776   Res. 94(D13), 16,287-16,301, doi: 10.1029/JD094iD13p16287, 1989.

777   Walter W. Immerzeel, Ludovicus P. H. van Beek, and Marc F. P. Bierkens.: Climate Change Will Affect

778   the Asian Water Towers, Science, 328, 1382-1385, doi: 10.1126/science.1183188, 2010.

779   Walvoord, M. A. and B. L. Kurylyk: Hydrologic Impacts of Thawing Permafrost—A Review, Vadose

780   Zone J., doi:10.2136/vzj2016.01.0010, 2016.

781   Walvoord, M. A., and R. G. Striegl: Increased groundwater to stream discharge from permafrost thawing

782   in the Yukon River basin: Potential impacts on lateral export of carbon and nitrogen, Geophys. Res.

783   Lett., 34, L12402, doi:10.1029/2007GL030216, 2007.

784   Wang, L., Koike, T., Yang, K., Jin, R., Li, H.: Frozen soil parameterization in a distributed biosphere

785   hydrological model, Hydrol. Earth Syst. Sc., 14(3), 557-571, doi: 10.5194/hess-14-557-2010, 2010.

786   Wang Q., Zhang T., Wu J., et al.: Investigation of permafrost distribution over the upper reaches of the

787   Heihe River in the Qilian Mountains, Journal of Glaciology and Geocryology, 35(1), 19-29, 2013

788   (in Chineses).

789   Wang Q., Zhang T., Peng X., Cao B., and Wu Q.: Changes of soil thermal regimes in the Heihe River

790   Basin over Western China, Arct., Antarct., and Alpine Res., 47(2), 231-241, doi:

791   10.1657/AAAR00C-14-012, 2015a.

792   Wang, Y., Yang, D., Lei, H. and Yang, H.: Impact of cryosphere hydrological processes on the river runoff

793   in the upper reaches of Heihe River, J. Hydraul. Eng., 46, 1064-1071, 2015b (In Chinese).

794   Wang, Y., Yang, H., Yang, D., Qin Y., Gao B. and Cong ZT.: Spatial interpolation of daily precipitation

795   in a high mountainous watershed based on gauge observations and a regional climate model

796   simulation, J. Hydrometeorol.,18, 845-862, 2017, doi: 10.1175/JHM-D-16-0089.1.

797   Woo, M.-K., Kane, D. L., Carey, S. K. and Yang, D.: Progress in permafrost hydrology in the new

798   millennium, Permafrost Periglac. Process., 19, 237-254, doi:10.1002/ppp.613, 2008.

799   Woo M K.: Permafrost Hydrology, Springer-Verlag, Berlin Heidelberg, 2012.

800   Wu, B.F., Yan, N.N., Xiong, J., Bastiaanssen, W., Zhu, W.W., Stein, A.: Validation of ETWatch using

801   field measurements at diverse landscapes: A case study in Hai Basin of China. J. Hydrol., 436, 67-

802   80, doi: 10.1016/j.jhydrol.2012.02.043, 2012.

803   Wu, B.F.: Monthly Evapotranspiration Datasets (2000–2012) with 1 km Spatial Resolution over the

804   Heihe   River   Basin,   Heihe   Plan   Science   Data   Center   at   Lanzhou,   China,   doi:

805   10.3972/heihe.115.2013.db, 2013.

806   Wu, M., Jansson P. E., Tan X., Wu J., and Huang, J.: Constraining parameter uncertainty in simulations

807   of water and heat dynamics in seasonally frozen soil using limited observed data, Water, 8(2), 64,

808   doi:10.3390/w8020064, 2016.

809   Wu, Q., Zhang T. and Liu Y.: Permafrost temperatures and thickness on the Qinghai-Tibet Plateau, Glob.

810   Planet. Change, 72, 32-38, doi: 10.1016/j.gloplacha.2010.03.001, 2010.

811   Yang, D.W., Gao, B., Jiao, Y., Lei, H.M., Zhang, Y.L., Yang, H.B., Cong, Z.T.: A distributed scheme

812   developed for eco-hydrological modeling in the upper Heihe River, China Earth Sci., 58(1), 36-45,

813   doi: 10.1007/s11430-014-5029-7, 2015.

814   Yang, D.W., Herath, S., and Musiake, K.: Development of a geomorphology-based hydrological model

815   for large catchments, Annu. J. Hydraul. Eng., 42, 169-174, doi: 10.2208/prohe.42.169, 1998.

816   Yang, D.W., Herath, S., and Musiake, K.: A hillslope-based hydrological model using catchment area

817   and width functions, Hydrol. Sci. J., 47, 49-65, doi: 10.1080/02626660209492907, 2002.

818   Yang, M., F. E. Nelson, N. I. Shiklomanov, D. Guo, and G. Wan, Permafrost degradation and its

819   environmental effects on the Tibetan Plateau: A review of recent research, Earth Sci. Rev., 103, 31-

820   44, doi: 10.1016/j.earscirev.2010.07.002, 2010.

821   Ye, B., D. Yang, Z. Zhang, and D. L. Kane: Variation of hydrological regime with permafrost coverage

822   over Lena Basin in Siberia, J. Geophys. Res., 114, D07102, doi:10.1029/2008JD010537, 2009.

823   Zhao, L., C. L. Ping, D. Q. Yang, G. D. Cheng, Y. J. Ding, and S. Y. Liu: Changes of climate and

824   seasonally frozen ground over the past 30 years in Qinghai-Xizang (Tibetan) Plateau, China, Glob.

825   Planet. Change, 43, 19-31, doi: 10.1016/j.gloplacha.2004.02.003, 2004.

826   Zhang, Y.L., Cheng, G.D., Li, X., Han, X.J., Wang, L., Li, H.Y., Chang, X.L., Flerchinger, G.N.:

827   Coupling of a simultaneous heat and water model with a distributed hydrological model and

828   evaluation of the combined model in a cold region watershed, Hydrol. Process., 27(25), 3762-3776,

829   doi: 10.1002/hyp.9514, 2013.

830   Zhang, Y., Ohata, T., and Kadota, T.: Land-surface hydrological processes in the permafrost region of the

831   eastern Tibetan Plateau, J. Hydrol., 283, 41-56, doi: 10.1016/S0022-1694(03)00240-3, 2003.

832   Zhang, Y., X. Wang, R. Fraser, I. Olthof, W. Chen, D. Mclennan, S. Ponomarenko, and W. Wu: Modelling

833   and mapping climate change impacts on permafrost at high spatial resolution for an Arctic region

834   with complex terrain, The Cryosphere, 7, 1121-1137, doi:10.5194/tc-7-1121-2013, 2013.

835   Zhou, J.H. and Zheng, Y.R.: Vegetation Map of the upper Heihe basin, Version 2.0, Heihe Plan Science

836   Data Center at Lanzhou, China, doi:10.3972/heihe.426.2014.db, 2014.

837

838   **Figure caption:**

839   Figure 1. The Study area, hydrological stations, borehole observation and flux tower stations.

840   Figure 2. Model structure and vertical discretization of soil column.

841   Figure 3. Comparison of the simulated and the observed soil temperature at borehole observation

842   sites, and the observed data is provided by Wang et al. (2013).

843   Figure 4. Daily soil temperature at the Qilian station: (a) observation; (b) simulation; (c) difference

844   (simulation - observation).

845   Figure 5. Comparison of the simulated and observed daily frozen depths during the period of 2002-

846   2014 at: (a) the Qilian station, (b) the Yeniugou station.

847   Figure 6. Comparison of the simulated and the observed daily river discharge at: (a) the Yingluoxia

848   Gauge, (b) the Qilian Gauge, and (c) the Zhamashike Gauge. For each gauge, the upper and lower

849   panels show the calibration and validation periods, respectively. Nash-Sutcliffe efficiency and

850   relative error coefficients are indicated.

851   Figure 7. Simulated ground temperature changes in: (a) the freezing season (from November to

852   March) (b) the thawing season (from April to October). Results from linear regressions are indicated.

853   Figure 8. Change of the frozen soils in the upper Heihe basin: (a) areas of permafrost and basin

854   averaged annual air temperature; (b) the basin averaged annual maximum depths of seasonally

855   frozen ground and thaw above permafrost. Results from linear regressions are indicated.

856   Figure 9. Distribution of permafrost and seasonally frozen ground for two periods: (a) 1971-1980

857   and (b) 2001-2010; (c) Area where permafrost degraded to seasonally frozen ground from (a) to (b);

858   Percentage of permafrost area with respect to elevation on the (d) sunny and (e) the shaded slopes

859   for the two periods. Note that (d) and (e) share a legend.

860   Figure 10. Spatially averaged monthly ground temperatures simulated from 1971 to 2013 for two

861   elevation intervals: (a) seasonally frozen ground between 3300 and 3500 m; (b) permafrost that

862   degraded to seasonally frozen ground between 3500 and 3700 m.

863   Figure 11. Runoff and simulated evapotranspiration in (a) the freezing season and (b) the thawing

864   season for the period of 1971 to 2013. Trend lines are for simulated data and regression results are

865   shown. The upper two panels are for freezing season and the lower two panels are for thawing

866   season.

867   Figure 12. Basin averaged annual water storage (equivalent water depth) changes simulated over

868   the period of 1971 to 2013 for: (a) liquid water in the top layer of the ground (0-3 m); (b) ice in the

869   top layer of the ground (0-3 m); (c) and groundwater. Results from linear regressions are indicated.

870   Figure 13. Model simulated runoff showing changes from the 1971-1980 period to the 2001-2010

871   period with elevation for (a) the freezing season and (b) the thawing season, and (c) monthly

872   averaged seasonal runoff in permafrost and seasonally frozen ground for the period of 2001-2010.

873

874

875

876
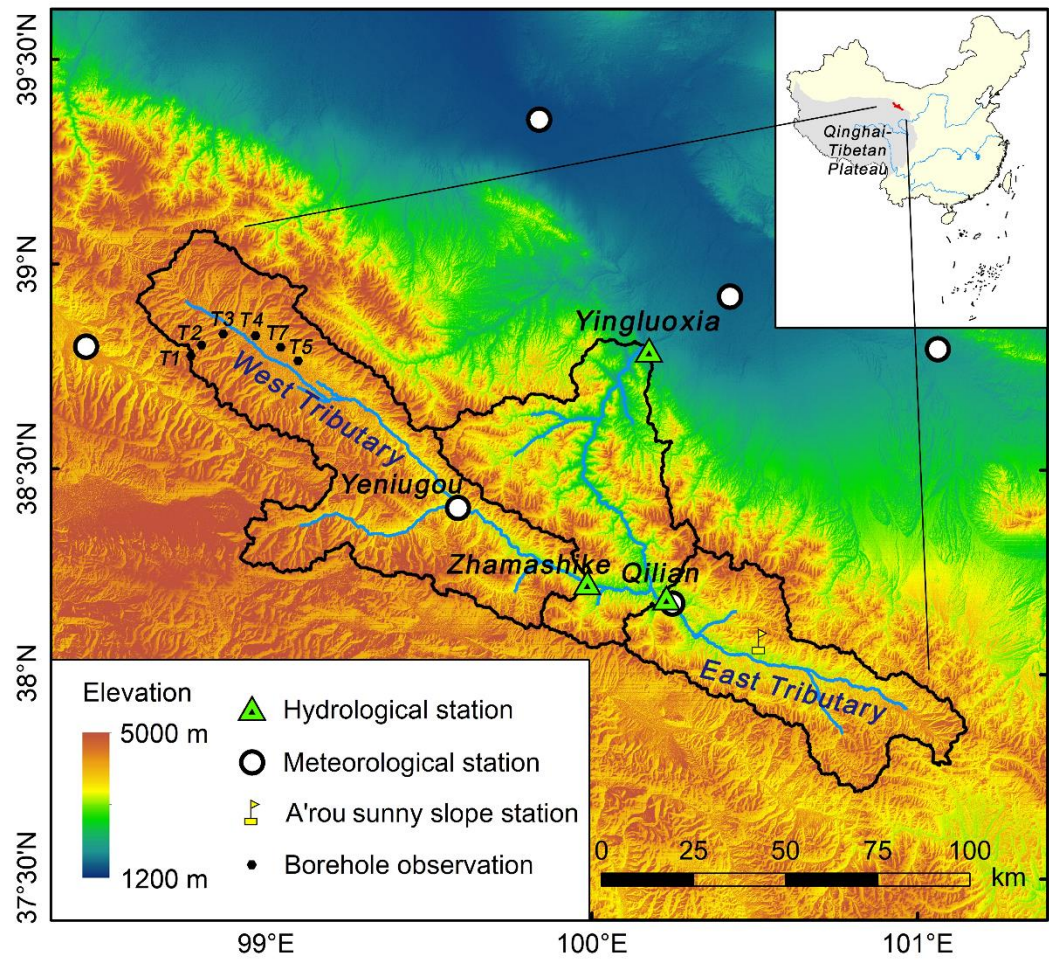
877

Figure 1. The Study area, hydrological stations, borehole observation and flux tower

stations.

880
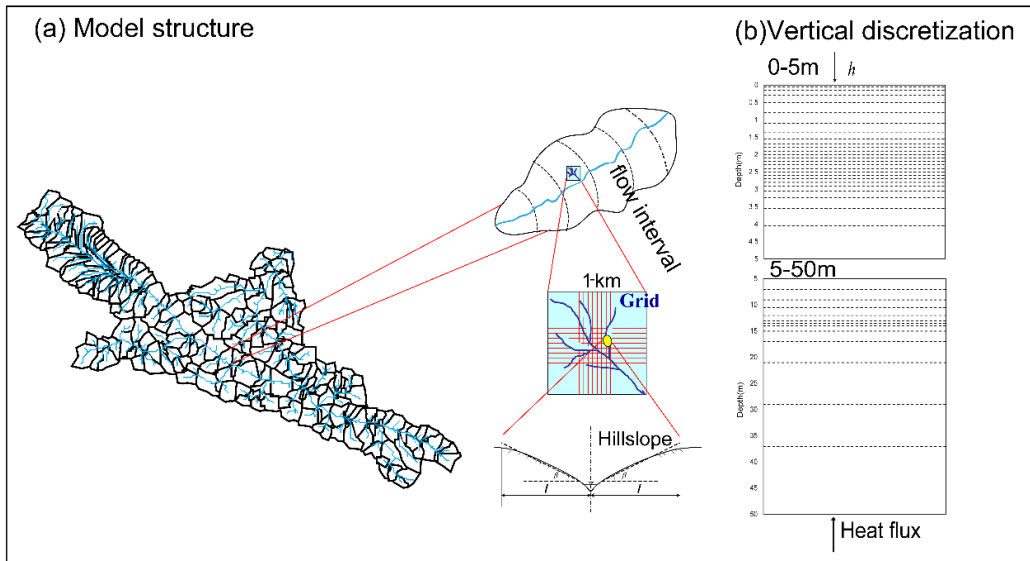
881

882   Figure 2. Model structure and vertical discretization of soil column.

883

884
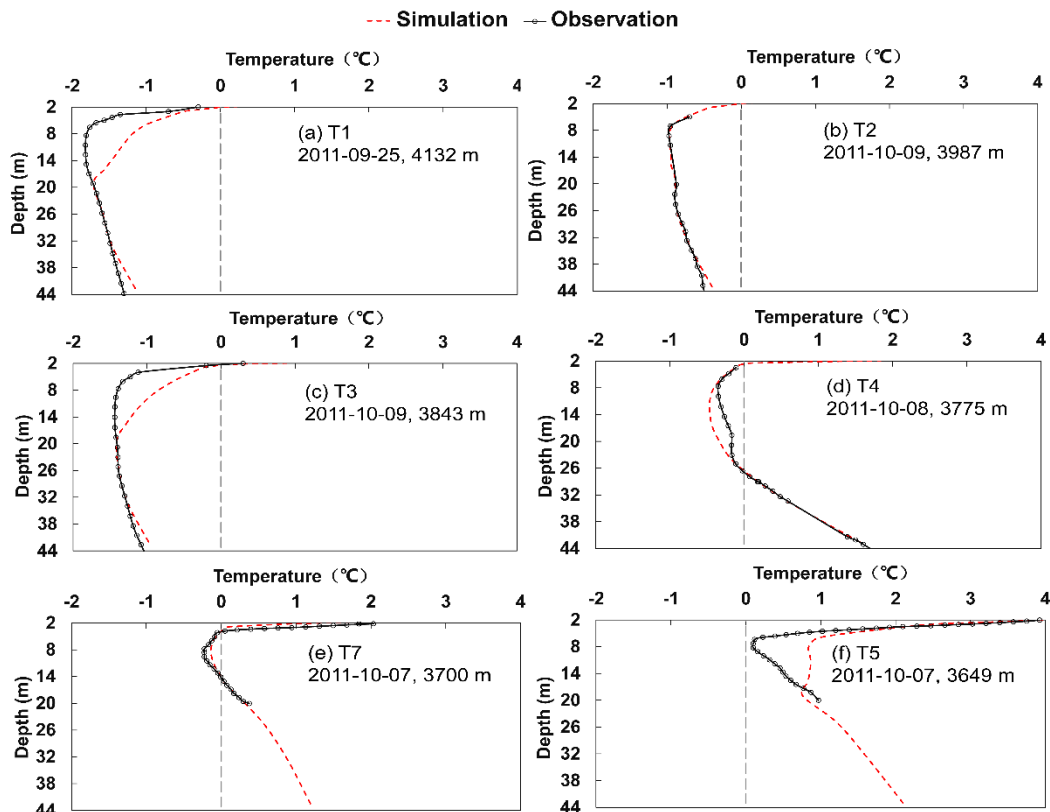
885

886   Figure 3. Comparison of the simulated and the observed soil temperature at borehole

887   observation sites, and the observed data is provided by Wang et al. (2013).
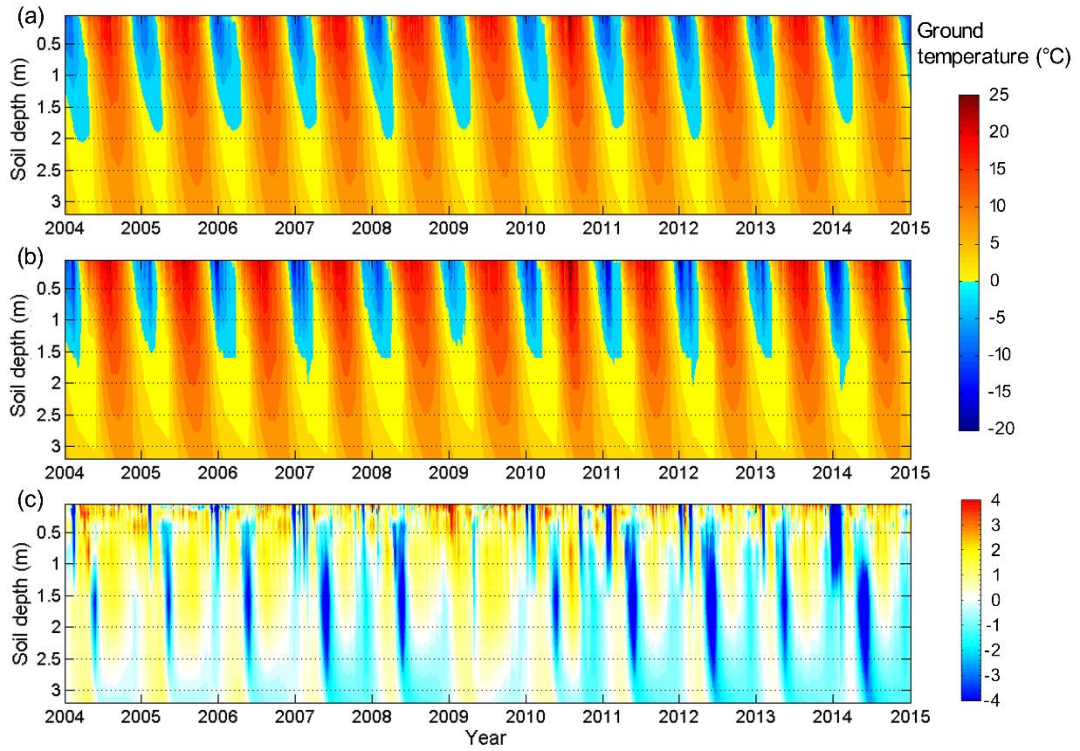
888

889   Figure 4. Daily soil temperature at the Qilian station: (a) observation; (b) simulation;

890   (c) difference (simulation - observation).

891

892
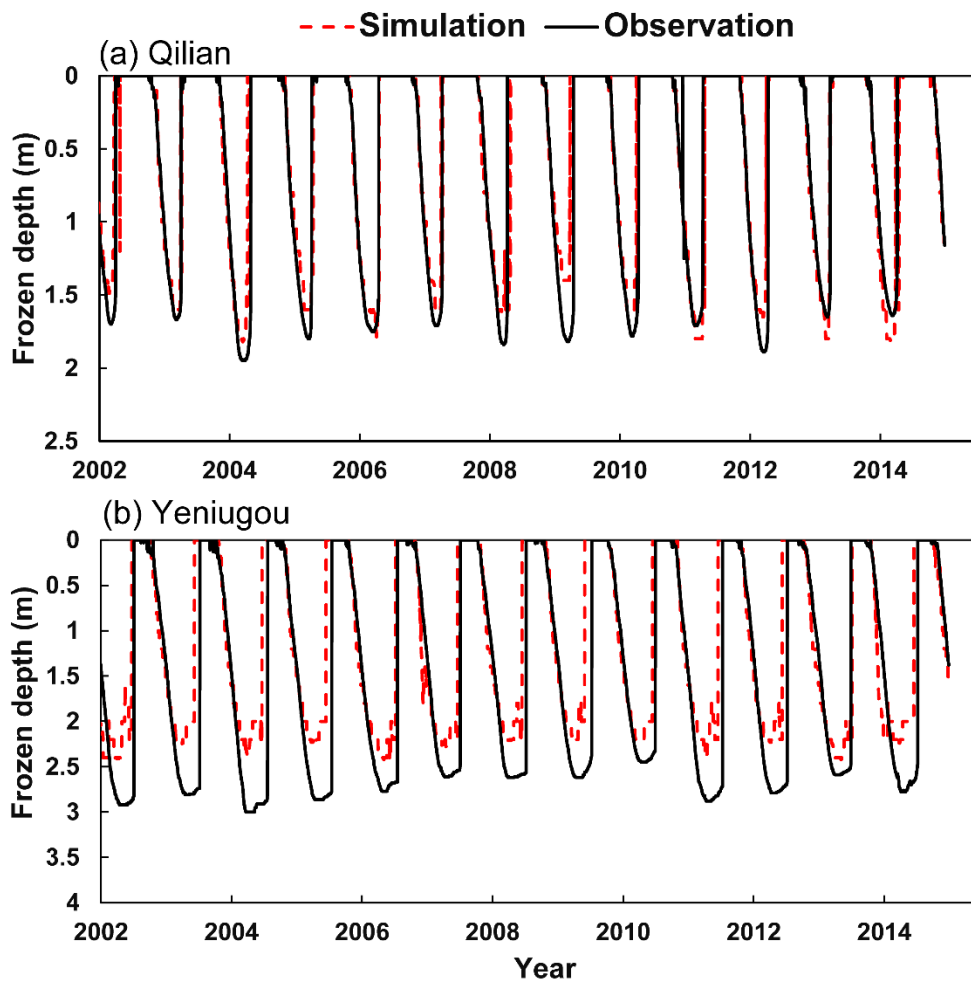
893

Figure 5. Comparison of the simulated and observed daily frozen depths during the

period of 2002-2014 at: (a) the Qilian station, (b) the Yeniugou station.

896

897
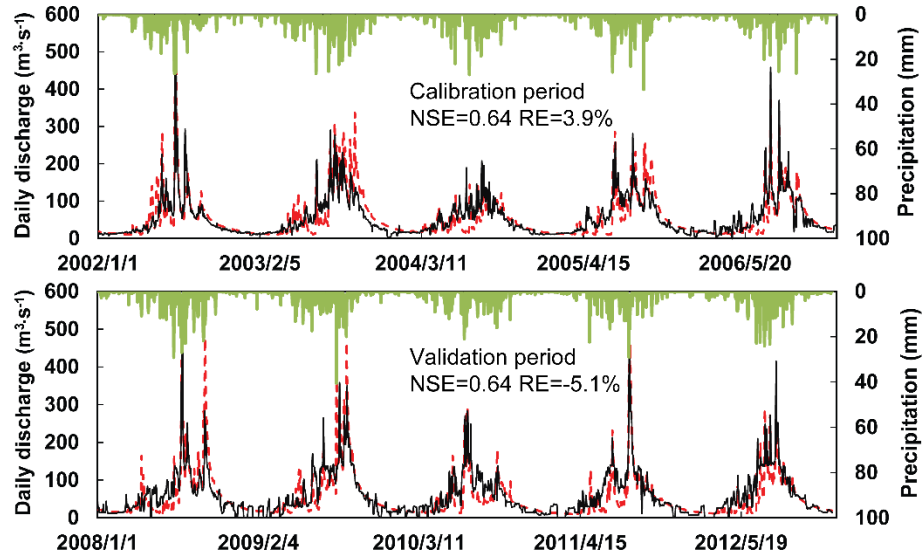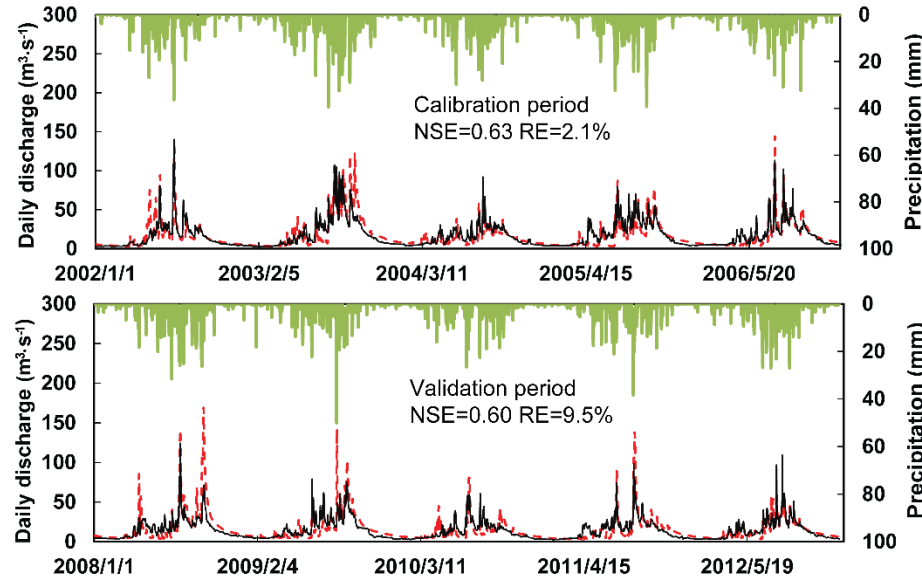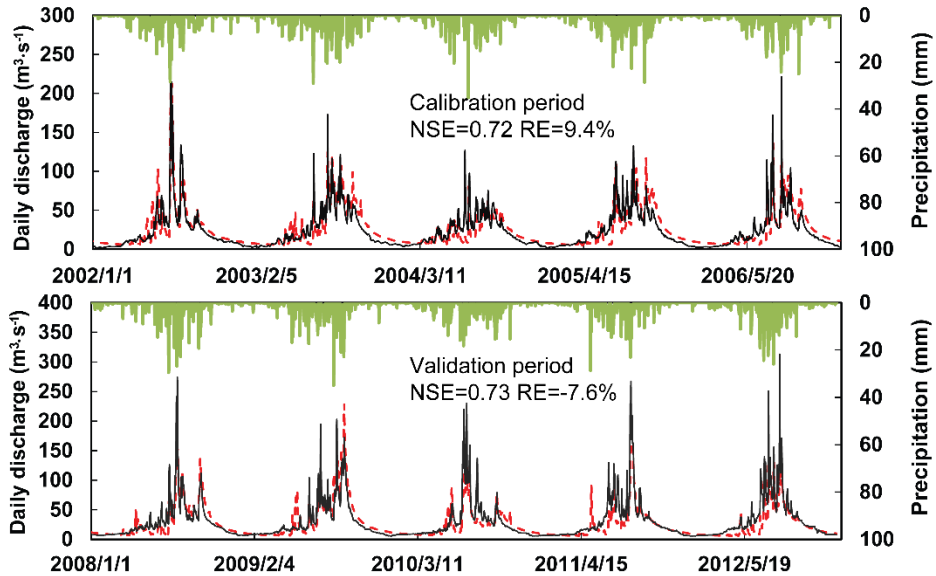
899   Figure 6. Comparison of the simulated and the observed daily river discharge at: (a) the

900   Yingluoxia Gauge, (b) the Qilian Gauge, and (c) the Zhamashike Gauge. For each

901   gauge, the upper and lower panels show the calibration and validation periods,

902   respectively. Nash-Sutcliffe efficiency and relative error coefficients are indicated.

903

904
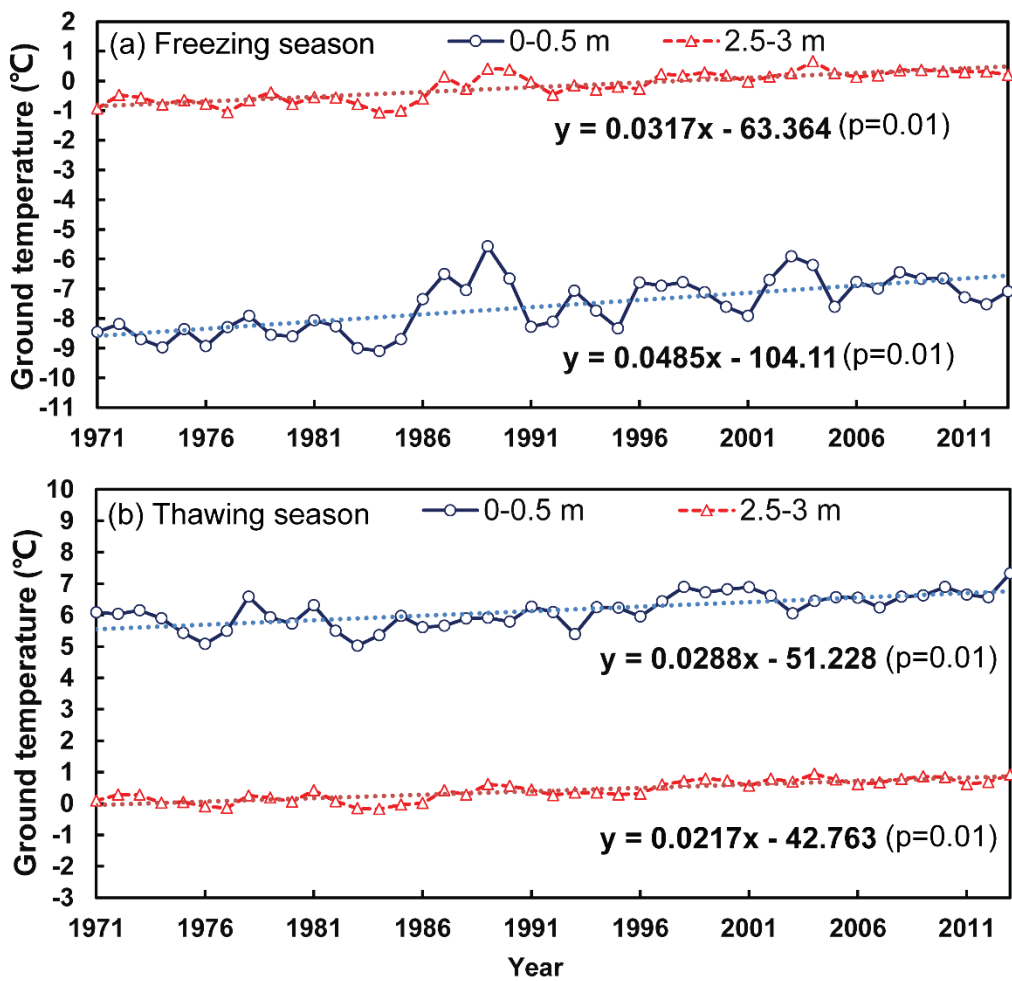
905

906   Figure 7. Simulated ground temperature changes in: (a) the freezing season (from

907   November to March) (b) the thawing season (from April to October). Results from

908   linear regressions are indicated.

909

910

911

912
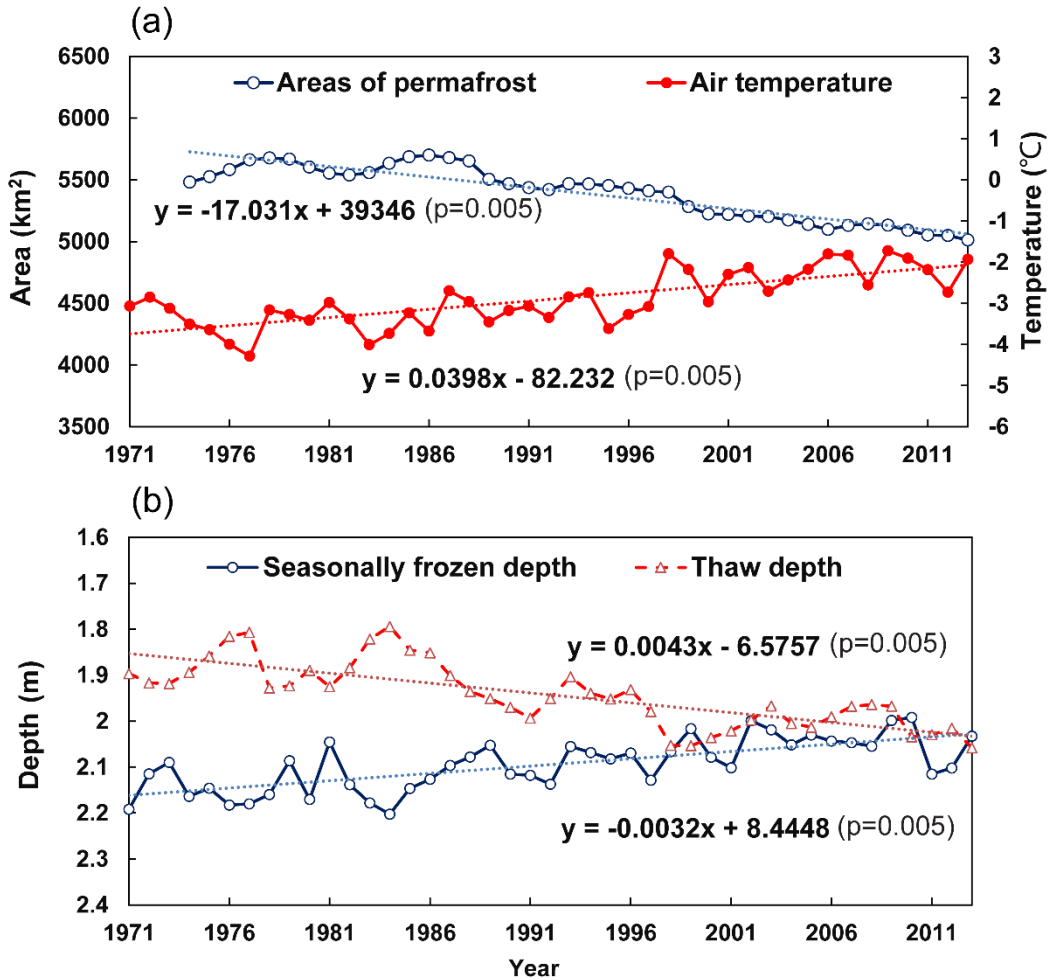
913

Figure 8. Change of the frozen soils in the upper Heihe basin: (a) areas of permafrost

and basin averaged annual air temperature; (b) the basin averaged annual maximum

depths of seasonally frozen ground and thaw above permafrost. Results from linear

regressions are indicated.

918

919
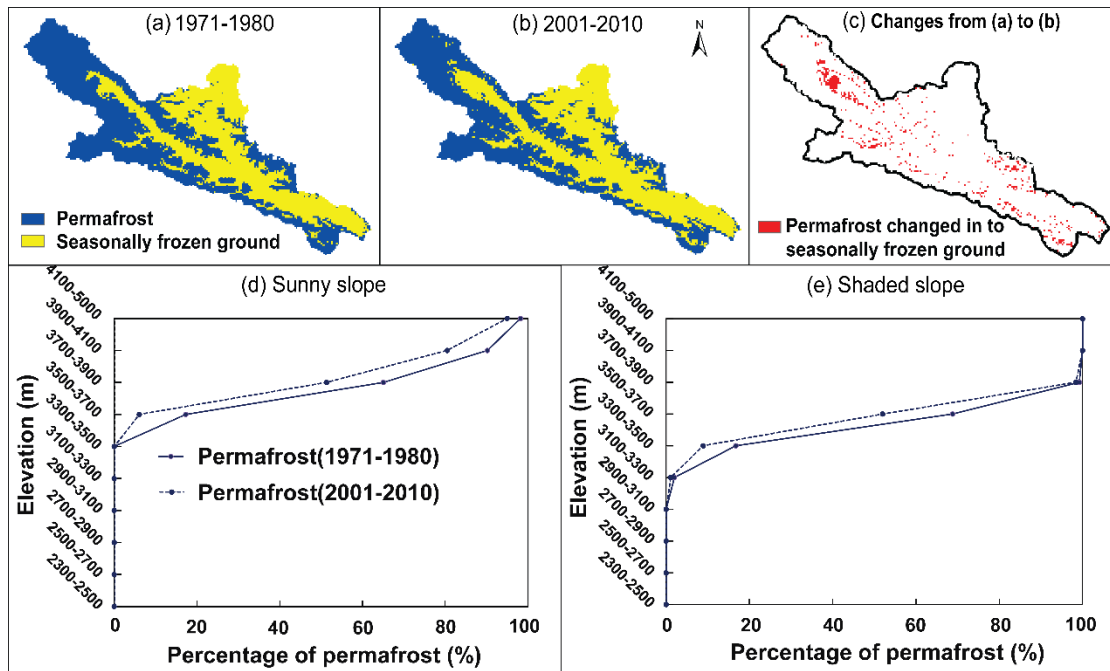
Figure 9. Distribution of permafrost and seasonally frozen ground for two periods: (a) 1971-1980 and (b) 2001-2010; (c) Area where permafrost degraded to seasonally frozen ground from (a) to (b); Percentage of permafrost area with respect to elevation on the (d) sunny and (e) the shaded slopes for the two periods. Note that (d) and (e) share a legend.
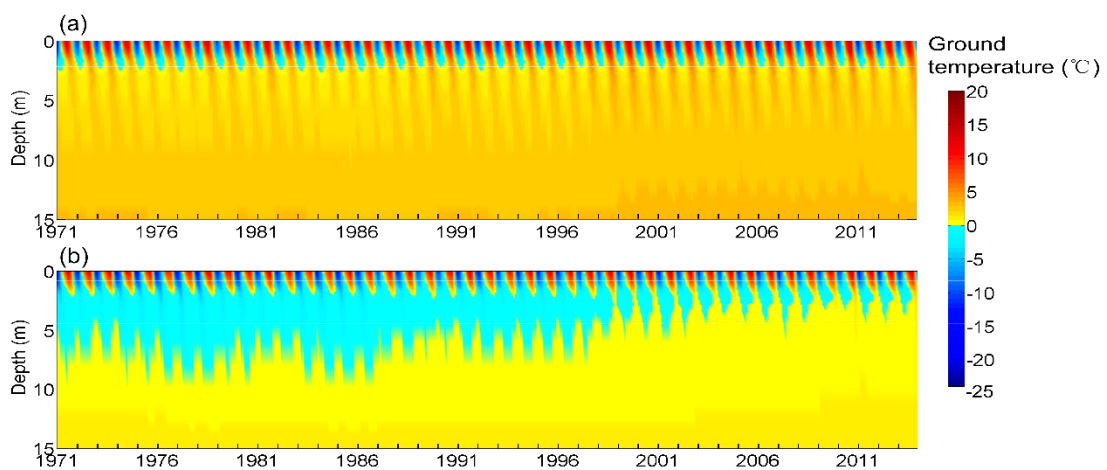
Figure 10. Spatially averaged monthly ground temperatures simulated from 1971 to 2013 for two elevation intervals: (a) seasonally frozen ground between 3300 and 3500 m; (b) permafrost that degraded to seasonally frozen ground between 3500 and 3700 m.

930

931
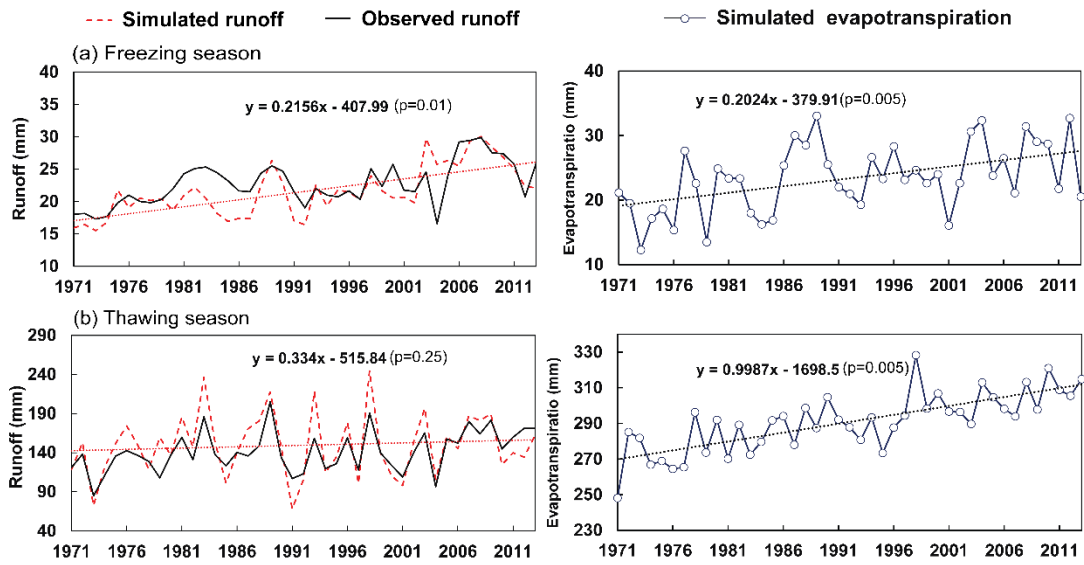
932

Figure 11. Runoff and simulated evapotranspiration in (a) the freezing season and (b)

the thawing season for the period of 1971 to 2013. Trend lines are for simulated data

and regression results are shown. The upper two panels are for freezing season and

the lower two panels are for thawing season.

937
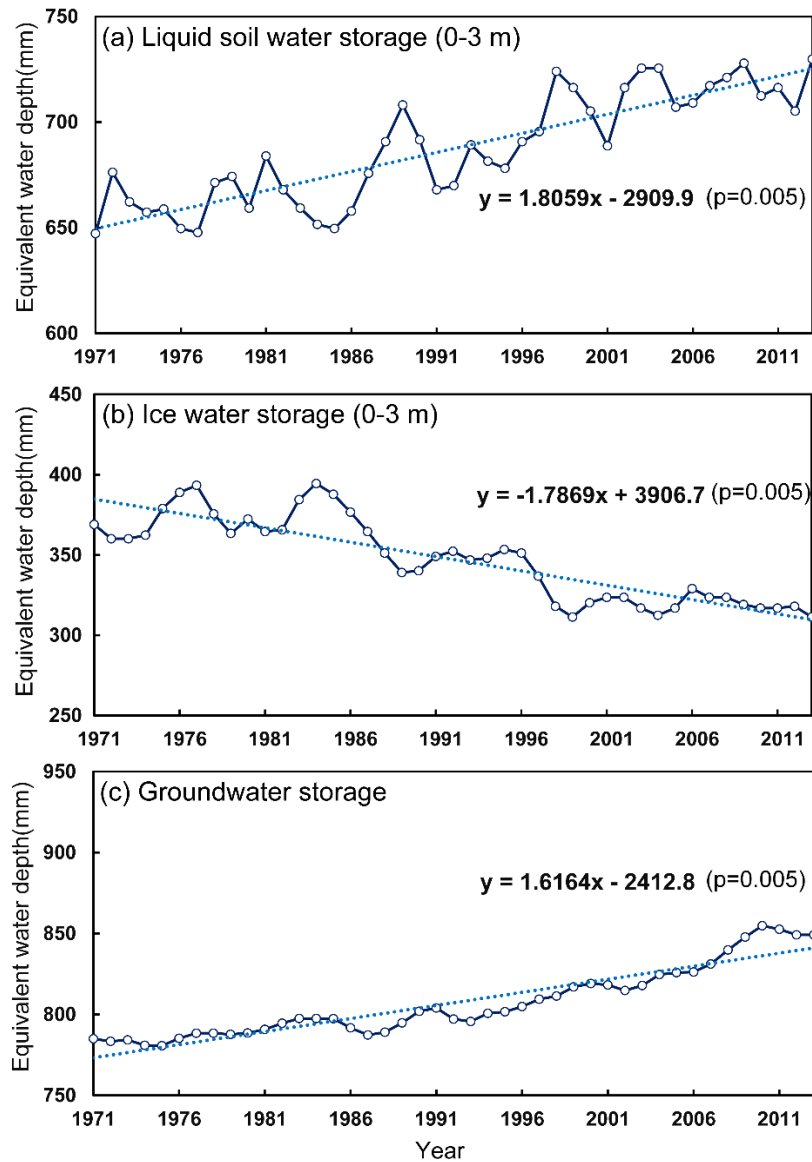
938

939   Figure 12. Basin averaged annual water storage (equivalent water depth) changes

940   simulated over the period of 1971 to 2013 for: (a) liquid water in the top layer of the

941   ground (0-3 m); (b) ice in the top layer of the ground (0-3 m); (c) and groundwater.

942   Results from linear regressions are indicated.
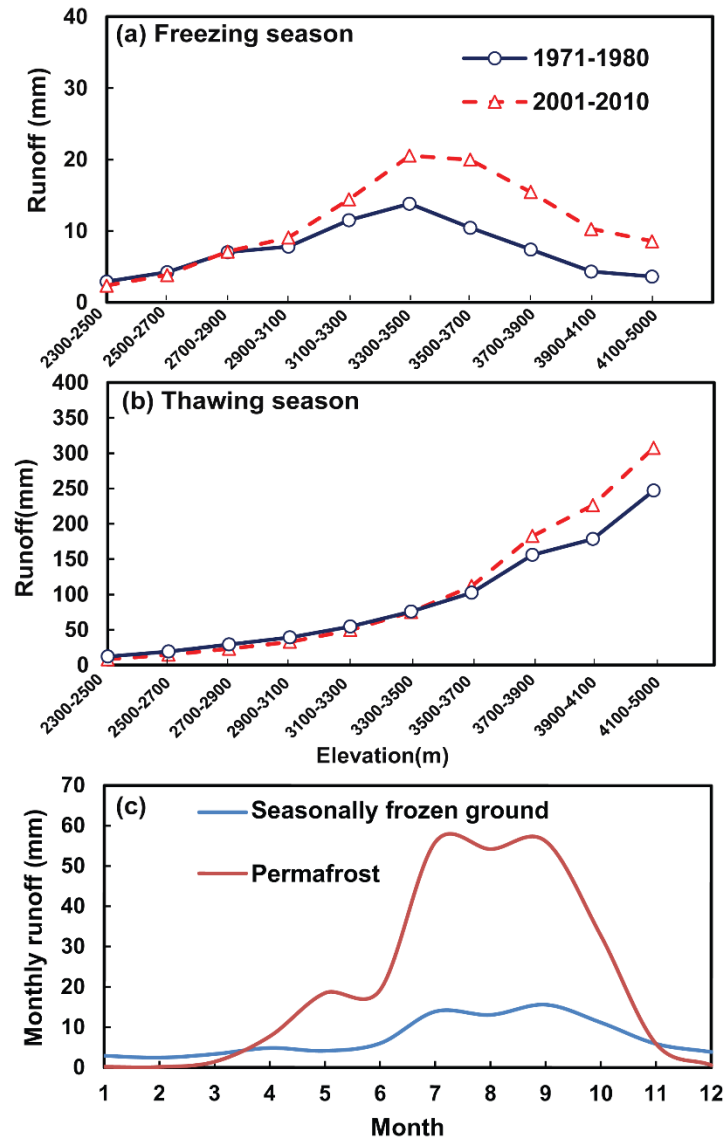
943

944   Figure 13. Model simulated runoff showing changes from the 1971-1980 period to the

945   2001-2010 period with elevation for (a) the freezing season and (b) the thawing

946   season, and (c) monthly averaged seasonal runoff in permafrost and seasonally frozen

947   ground for the period of 2001-2010.

948

949

950

951

952 **Table list:**

953 Table 1. Major parameters of the GBEHM model.

954 Table 2. Changes in annual basin water balance and runoff components (mm·y^{-1}) in different seasons.

955

956   Table 1. Major parameters of the GBEHM model.

Parameters	Coniferous Forest	Shrub	Steppe	Alpine Meadow	Alpine Sparse Vegetation	Desert
Surface retention capacity (mm)	30.0	25.0	10.0	15.0	15.0	5.0
Surface roughness (Manning coefficient)	0.5	0.3	0.1	0.1	0.1	1.0
Soil reflectance to visible light	0.20	0.20	0.20	0.28	0.14	0.11
Soil reflectance to near-infrared radiation	0.225	0.225	0.225	0.28	0.225	0.225
Leaf reflectance to visible light	0.105	0.105	0.105	0.105	0.105	—
Leaf reflectance to near-infrared radiation	0.35	0.58	0.58	0.58	0.58	—
Leaf transmittance to visible light	0.05	0.07	0.07	0.07	0.07	—
Leaf transmittance to near-infrared radiation	0.10	0.25	0.25	0.25	0.25	—
Maximum Rubsico capacity of top leaf (10^{-5} mol·m^{-2}·s^{-1})	6.0	6.0	3.3	3.3	3.0	—
Plant root depth (m)	2.0	1.0	0.40	0.40	0.1	0.0
Intrinsic quantum efficiency (mol·mol^{-1})	0.08	0.08	0.05	0.05	0.05	—
Canopy top height (m)	9.0	1.9	0.3	0.3	0.2	—
Leaf length (m)	0.055	0.055	0.3	0.3	0.04	—
Leaf width (m)	0.001	0.001	0.005	0.005	0.001	—
Stem area index	0.08	0.08	0.05	0.05	0.08	—

957   Table 2. Changes in annual basin water balance and runoff components (mm·y^{-1}) in different seasons.

Decade	P	E	Sim R	Obs R	Runoff ratio (Obs)	Runoff ratio (Sim)	Freezing season (from November to March)			Thawing season (from April to October)		
							T	G	S	T	G	S
1971-1980	439.1	282.1	154.1	143.8	0.33	0.35	18.5	0.0	0.0	135.6	3.5	13.8
1981-1990	492.8	300.8	188.5	174.1	0.35	0.38	20.5	0.0	0.0	168.0	3.1	27.8
1991-2000	471.0	307.6	161.9	157.4	0.33	0.34	20.5	0.0	0.0	141.4	3.8	18.4
2001-2010	504.3	319.0	180.6	174.3	0.35	0.36	26.2	0.0	0.0	154.3	3.7	24.1

958   Note: P means precipitation, E means actual evaporation, R means runoff, T means total runoff, G

959   means glacier runoff and S means snowmelt runoff, Sim means simulation and Obs means

960   observation.